

## AN ABSTRACT OF THE THESIS OF

Robert L. Thuemler for the degree of Master of Science in Electrical and Computer Engineering presented on May 28, 1997. Title: Characterization of Alternating-Current Thin-Film SrS:Ce Electroluminescent Devices.

Abstract approved:

*Redacted for Privacy*

---

John F. Wager

The electrical characteristics of several different kinds of SrS:Ce alternating-current thin-film electroluminescent (ACTFEL) devices are compared and contrasted to an evaporated ZnS:Mn ACTFEL device using capacitance-voltage (C-V) and internal charge-phosphor field (Q-F<sub>p</sub>) analysis techniques. Evaporated ZnS:Mn ACTFEL devices exhibit nearly ideal electrical characteristics in which the physics of device operation is relatively well established. In contrast, SrS:Ce ACTFEL devices exhibit characteristics that are not explained by simply invoking the same device physics considerations that apply to ZnS:Mn ACTFEL devices. SrS:Ce ACTFEL device physics is dominated by dynamic space charge effects caused by ionization of Ce and other native defects in the host phosphor. Dynamic space charge exhibits itself in the electrical curves that are used to characterize ACTFEL devices as a distortion compared to curves which exhibit no dynamic space charge. The exact nature of native defects in SrS:Ce ACTFEL devices is not well established. The transient thermoluminescent (TTL) experiment is successfully set up and is used to add to the knowledge of these defects by characterizing the activation energy of observed traps. Previous TTL work has only reported the activation energy of observed traps and has been carried out on electron beam (e-beam) evaporated SrS:Ce thin-films up to a temperature of 430 K while the work reported herein investigates the TTL response of sputtered and atomic-

layer epitaxy (ALE) deposited SrS:Ce ACTFEL devices up to a temperature of 560 K and adds capture cross-section information. TTL analysis demonstrates that trap activation energies and capture cross-sections can be estimated. The deep-level transient spectroscopy (DLTS) rate-window concept is applied to the analysis of TTL data and is shown to provide consistent results. TTL analysis may prove to be of importance in establishing the nature of traps in SrS ACTFEL devices processed in various manners and for the analysis of traps in other phosphor materials used for ACTFEL devices.

© Copyright by Robert L. Thuemler

May 28, 1997

All Rights Reserved

Characterization of Alternating-Current Thin-Film SrS:Ce Electroluminescent Devices

by

Robert L. Thuemler

A THESIS

submitted to

Oregon State University

in partial fulfillment of  
the requirements for the  
degree of

Master of Science

Presented May 28, 1997

Commencement June 1998

Master of Science thesis of Robert L. Thuemler presented on May 28, 1997

APPROVED:

*Redacted for Privacy*

---

Major Professor, representing Electrical and Computer Engineering

*Redacted for Privacy*

---

Head of Department of Electrical and Computer Engineering

*Redacted for Privacy*

---

Dean of Graduate School *J*

I understand that my thesis will become part of the permanent collection of Oregon State University libraries. My signature below authorizes release of my thesis to any reader upon request.

*Redacted for Privacy*

---

Robert L. Thuemler, Author

## ACKNOWLEDGEMENTS

Foremost, I would like to thank my wife, Tamara Thuemler, and our children for their support and encouragement throughout the duration of this research, without which none of this would have been possible and to whom this thesis is dedicated.

Furthermore, I would like to thank Dr. Wager for his many discussions and for providing much opportunity for technical and personal growth.

I would like to thank all of the researchers in the EL group with whom I have had many fruitful discussions during the course of this research.

Acknowledgment is given to Juha Viljanen and Erkki Soininen of Planar International for providing atomic-layer epitaxy (ALE) SrS:Ce ACTFEL devices, Phillip Bailey of Westaim Corporation for providing electron-beam evaporated SrS:Ce ACTFEL devices, John Samuels of Los Alamos National Laboratories for providing metal-organic chemical vapor deposition (MOCVD) SrS:Ce ACTFEL devices, and Sey-Shing Sun and Tin Nguyen of Planar America for providing sputtered SrS:Ce ACTFEL devices.

This work is supported by the U.S. Army Research Office under Contract No. DAAH04-94-G-0324 and by the Defense Advanced Research Projects Agency under the Phosphor Technology Center of Excellence, Grant No. MDA 972-93-1-0030.

## TABLE OF CONTENTS

	Page
Chapter 1 INTRODUCTION.....	1
Chapter 2 LITERATURE REVIEW.....	3
2.1 History and Background of ACTFEL Devices.....	3
2.2 Device Structure.....	3
2.3 Device Fabrication.....	5
2.4 Device Operation.....	7
2.5 Dynamic Space Charge in an ACTFEL Device.....	10
2.6 Device Modeling.....	12
Chapter 3 ELECTRICAL EXPERIMENTAL TECHNIQUES.....	14
3.1 Experimental Setup.....	14
3.2 Capacitance-Voltage (C-V) Analysis.....	14
3.3 External Charge-Voltage (Q-V) Analysis.....	16
3.4 Internal Charge-Phosphor Field (Q-F <sub>p</sub> ) Analysis.....	18
3.5 Experimental Limitations and Sample Preparation.....	21
3.5.1 Effect of Current-Limiting Resistor.....	21
3.5.2 Effect of Measured Voltage Offset.....	22
3.6 Dynamic Space Charge Effects.....	23
Chapter 4 ELECTRICAL CHARACTERIZATION OF SrS:Ce DEVICES.....	25
4.1 Capacitance - Voltage Experimental Results.....	25
4.2 Internal Charge-Phosphor Field (Q-F <sub>p</sub> ) Experimental Results.....	28
4.3 Phosphor Field - Thickness Dependence.....	32

## TABLE OF CONTENTS (CONTINUED)

	Page
4.4 Electrical Characteristics of Undoped ALE SrS.....	35
4.5 Conclusion .....	36
Chapter 5 TRANSIENT THERMOLUMINESCENCE.....	38
5.1 Introduction.....	38
5.2 Transient Thermoluminescence Experimental Setup .....	43
5.3 Transient Thermoluminescence Experimental Results.....	44
5.4 Rate-Window Analysis of the Luminescent Decay Curves.....	48
5.5 Summary .....	52
Chapter 6 CONCLUSIONS AND RECOMMENDATIONS FOR FUTURE WORK .....	54
6.1 Conclusions.....	54
6.2 Recommendations for Future Work.....	55
BIBLIOGRAPHY.....	57

## LIST OF FIGURES

<u>Figure</u>		<u>Page</u>
2.1	Typical ACTFEL device structure.....	4
2.2	Inverted ACTFEL device structure.....	5
2.3	Standard ACTFEL driving waveform.....	7
2.4	Cycle of energy band diagrams.....	9
2.5	Energy band bending (a) without space charge, and (b) with positive space charge. ....	11
2.6	Simple ACTFEL equivalent circuit. ....	12
3.1	Electrical circuit used to characterize ACTFEL devices. ....	15
3.2	Typical C-V curve for an evaporated ZnS:Mn ACTFEL device with no dynamic space charge. ....	16
3.3	Typical Q-V plot for evaporated ZnS:Mn EL ACTFEL device with no dynamic space charge. ....	17
3.4	Typical Q-F <sub>p</sub> plot for evaporated ZnS:Mn EL ACTFEL device with no dynamic space charge. ....	18
3.5	A typical Q-V curve for a SrS:Ce ACTFEL device with dynamic space charge. Only the positive pulse is shown for clarity. ....	19
3.6	A set of Q-F <sub>p</sub> curves for a SrS:Ce ACTFEL device with dynamic space charge using the values of C <sub>i</sub> as determined from the Q-V curve in Fig. 3.5. ....	20
3.7	V(t) showing deviations from an ideal curve as the current-limiting resistance increases. ....	22
3.8	C-V curves showing distortion as a result of the magnitude of the current-limiting resistor. ....	23
3.9	Example of Q-F <sub>p</sub> curve shift due to offset voltage on C <sub>s</sub> . ....	24
4.1	C-V curves for an evaporated ZnS:Mn ACTFEL device with the Al electrode positively biased. ....	25

## LIST OF FIGURES (CONTINUED)

<u>Figure</u>		<u>Page</u>
4.2	Positive polarity C-V curves for (a) ALE SrS:Ce, (b) sputtered SrS:Ce, (c) e-beam evaporated SrS:Ce, and (d) MOCVD SrS:Ce ACTFEL devices. ....	26
4.3	Negative polarity C-V curves for (a) ALE SrS:Ce, (b) sputtered SrS:Ce, (c) e-beam evaporated SrS:Ce, and (d) MOCVD SrS:Ce ACTFEL devices. ....	27
4.4	Q-F <sub>p</sub> curves for an evaporated ZnS:Mn ACTFEL device.....	29
4.5	Q-F <sub>p</sub> curves for (a) ALE SrS:Ce, (b) sputtered SrS:Ce, (c) e-beam evaporated SrS:Ce, and (d) MOCVD SrS:Ce ACTFEL devices.....	30
4.6	Cycle of energy band diagrams for a SrS:Ce ACTFEL device for a single polarity. The heavy dashed line represents a return to the state depicted in (b) through a similar cycle of energy band diagrams for the opposite polarity pulse.....	31
4.7	Q-F <sub>p</sub> curves for (a) ALE SrS:Ce and (b) sputtered SrS:Ce ACTFEL devices taken at 60 V over threshold which show the phosphor field dependence on thickness. ....	33
4.8	Dependence of phosphor field on thickness based on the values given in Table 4.1. ....	34
4.9	Energy band diagrams for (a) a thin SrS:Ce ACTFEL device and (b) a thick SrS:Ce ACTFEL device. ....	35
4.10	Q-F <sub>p</sub> curves for an undoped ALE SrS sample. ....	36
5.1	Thermal interactions between traps and band edges.....	39
5.2	Simplified model of a luminescent material with one electron trapping state.....	40
5.3	Basic TTL experimental setup. ....	43
5.4	TTL response curves for an undoped, (i.e. no Ce) sputtered SrS ACTFEL device which is doped with Ga. The curves from bottom to top are for sampling time $t_s = 999$ ms, 500 ms, 250ms, 100 ms, 50 ms, 30 ms, and 15 ms. The top most curve is the steady-state luminescence $I_0$ . ....	44

## LIST OF FIGURES (CONTINUED)

<u>Figure</u>		<u>Page</u>
5.5	Arrhenius plots of the peaks seen in the TTL response curves from Fig. 5.4 for the peaks occurring at (a) 250 K and (b) 400 K.....	45
5.6	TTL response curves for an ALE SrS:Ce ACTFEL device. The curves from bottom to top are for sampling time $t_s = 999$ ms, 500 ms, 250ms, 100 ms, 50 ms, 30 ms, and 15 ms. The top most curve is the steady-state luminescence $I_0$ .....	46
5.7	Arrhenius plot of the peak seen in the TTL response curves from Fig. 5.6 occurring at 450 K. ....	47
5.8	Rate-window curves for an undoped sputtered SrS with Ga codoping ACTFEL device. These curves were constructed using a constant $t_1:t_2$ ratio of 1:10. The curves from top to bottom are for $t_1:t_2$ times of 10:100, 20:200, 30:300, 40:400, 50:500, 60:600, 70:700. ....	49
5.9	Arrhenius plots of the peaks seen in the rate-window curves from Fig. 5.8 for the peaks occurring at (a) 300 K and (b) 425 K.....	50
5.10	Rate-window curves for an ALE SrS:Ce ACTFEL device. These curves were constructed using a constant $t_1:t_2$ ratio of 1:10. The curves from top to bottom are for $t_1:t_2$ times of 15:150, 20:200, 30:300, 40:400, 50:500, 60:600, 70:700, 80:800.....	51

## LIST OF TABLES

<u>Table</u>		<u>Page</u>
2.1	List of characterized SrS materials. ....	6
4.1	A comparison of $V_{th}$ and $F_{peak}$ for SrS:Ce ACTFEL devices with varying thicknesses. ....	34

# Characterization of Alternating-Current Thin-Film SrS:Ce Electroluminescent Devices

## Chapter 1 INTRODUCTION

Display technology is being steadily driven towards light-weight, high-quality, high-resolution displays to replace the current cathode ray tube (CRT) display. Among the display driving forces are the advancement of portable computers, high-definition television (HDTV), and head-mounted displays. Flat panel display (FPD) technology is the CRT replacement technology of choice.

FPD's are categorized based on the physical phenomenon that they utilize to produce light. The current FPD's are plasma, liquid crystal (LCD), field emission (FED), and electroluminescent (EL) displays. Each of these display types has unique advantages and disadvantages that allow them to be suited for particular markets. Plasma, FED, and EL display technologies are based on the process that converts electrical energy to luminous energy. There have been many roadblocks to the commercial success of electroluminescence, thus enabling other technologies, such as LCD, to take pre-eminence in the flat panel world despite drawbacks such as limited viewing angle and the requirements of an external light source.

EL displays are among the most promising of the FPD technologies. This is due to the emissive nature of the display which gives it a wide viewing angle, high brightness, and high contrast. Of the roadblocks that remain in the development of a commercial EL display technology, the most vexing one has been the inability to produce a high quality blue phosphor.

There have been several promising blue phosphors, but each has exhibited some weakness making it unsuitable for use in EL displays. SrS:Ce was first investigated for use in EL displays in the 1980's [1], although it had been known as a blue phosphor since the late 1950's [2]. At that time its aging stability proved to be the critical limiting factor and the phosphor was quickly discarded. Blue phosphor development

continued via exploration of thiogallate-based phosphors [3, 4, 5]. These materials have proven to yield a good blue color as well as exhibiting excellent aging stability. However, these phosphors have low brightness and low efficiency, while operating at fields in excess of those required for portable FPD's. This class of blue phosphors has now been replaced by a renewed interest in the SrS:Ce phosphor.

The re-emergence of the SrS:Ce phosphor as the current dominant EL blue phosphor is due to several factors. Better processing, resulting in a high-quality SrS host lattice, has led to an aging stability that is approaching an acceptable duration for display purposes. Great strides have been made in understanding the underlying physics of how this phosphor operates. Space charge, which was once thought to be the death knell of any viable EL phosphor, has proven to be the saving characteristic that allows this phosphor to be appropriate for EL technology.

The focus of this thesis is to explore methods of enhancing the basic understanding of the physics and chemistry of the SrS:Ce phosphor. In particular, the primary emphasis of this thesis is in exploring space charge using methods of determining the energy levels of the defects that cause space charge to be generated within the phosphor. Since processing has played such a critical role in bringing SrS:Ce back to the forefront of blue EL phosphor research, a comparison is made wherever possible between the characteristics exhibited by SrS:Ce grown by several different methods.

The organization of this thesis is broken into segments, each of which covers a specific topic. Chapter 2 is a review of relevant literature that covers the fundamental physics of alternating-current thin-film electroluminescent (ACTFEL) phosphors. Chapter 3 covers the experimental techniques used to gather and analyze electrical data used in this study. Chapter 4 focuses on the electrical characteristics of SrS:Ce samples grown by various deposition methods. Chapter 5 contains the experimental details and results of the transient-thermoluminescence (TTL) experiment and applies the deep-level transient spectroscopy (DLTS) rate-window approach to the luminescent decay curve. Finally, Chapter 6 gives conclusions and recommendations for future research.

## Chapter 2

# LITERATURE REVIEW

This chapter contains essential background information regarding ACTFEL devices and an overview of literature covering previous SrS:Ce research.

### 2.1 History and Background of ACTFEL Devices

Electroluminescence (EL) is a phenomenon whereby electrical energy is transformed into light or optical energy. EL was discovered in 1936 when emission of light from a ZnS phosphor powder dispersed in an insulator that was sandwiched between two electrodes was observed [6]. The double-insulating layer structure, such as that used throughout this thesis, was first reported in 1967 [7] and is currently used for all commercial EL displays. This double-insulating structure was used to develop a ZnS:Mn device with a luminance of 1000 fL at a 5 kHz driving frequency and a lifetime of greater than 10,000 hours [8]. This breakthrough resulted in ACTFEL displays becoming viable for commercial applications.

Optical probing of the electronic transitions of Ce in a crystalline structure was first reported in 1931 [9]. Basic research into the physical properties of SrS:Ce, such as bandgap energy, was not carried out until the late 1950's [2, 10] due largely to difficulties in growing pure crystals. The announcement of SrS:Ce as a possible blue ACTFEL phosphor in 1984 [1] created a flurry of investigation of this material that is currently still very active.

### 2.2 Device Structure

The general structure of an ACTFEL device is illustrated in Fig. 2.1. As shown in Fig. 2.1, the active portion of an ACTFEL device is deposited on a glass substrate. The active portion of an ACTFEL device consists of a phosphor layer sandwiched between two insulating layers that are contacted by separate electrodes. The standard

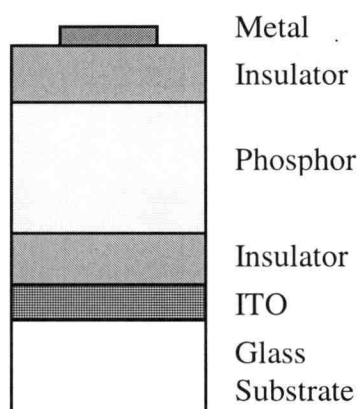


**Figure 2.1** Typical ACTFEL device structure.

material used for the bottom electrode is indium tin oxide (ITO) because it is transparent in the visible spectrum and is a relatively good conductor. The most common ACTFEL insulator layers are aluminum titanium oxide (ATO), silicon oxynitride (SiON), or barium tantalate oxide (BTO) although other novel materials can be used. These materials are chosen because they have high dielectric constants and a high resistance to electrical breakdown.

The phosphor host material used in this study is SrS. The host material is doped with a luminescent impurity that gives rise to photon emission when excited by a carrier. In this study, cerium in strontium sulphide (SrS:Ce) is used as the impurity to yield blue-green photons. Finally, the top electrode of most ACTFEL devices is metal, usually aluminum. This structure comprises the largest class of ACTFEL devices and is termed a normal ACTFEL stack. Light generated in the phosphor layer exits the deposited stack through the glass substrate.

Some of the devices used in this study are fabricated with an inverted stack which is illustrated in Fig. 2.2. In this structure the substrate is usually a ceramic material. The bottom electrode in this configuration is a metal, generally gold, while the top electrode is fabricated from ITO. Novel insulators are typically used in this structure because of the high-temperature processing capability provided by ceramics. The phosphor used in inverted devices for this study is SrS:Ce. Light generated in the phosphor layer in this configuration exits through the top ITO layer.

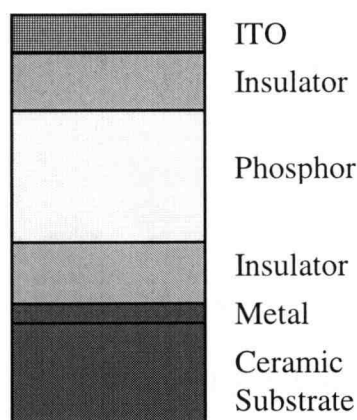


**Figure 2.2** Inverted ACTFEL device structure.

### 2.3 Device Fabrication

The fabrication of an ACTFEL device involves deposition of the electrodes, insulators, and the phosphor layer onto a suitable substrate. Many deposition methods have been used in ACTFEL device fabrication but the most commonly used can be separated into two types of process techniques: physical vapor deposition (PVD) and chemical vapor deposition (CVD). Sputtering, electron-beam evaporation, and multi-source reactive evaporation are examples of PVD. Atomic layer epitaxy (ALE) and metal-organic CVD (MOCVD) fall into the CVD category. Previous research has shown that the method of deposition of the ACTFEL device has a significant effect on both the electrical and optical characteristics of the device [11,12,13].

Sputtering is a process in which gas ions from a plasma are accelerated toward, and strike a target material transferring the kinetic energy of the ion to the target [14]. Target atoms are then sputtered (ejected) from the target surface and are transported to the substrate where they condense to form a thin-film.

Evaporation is a process where thermal energy is used to cause evaporation of atoms from a target [15]. In electron-beam (e-beam) evaporation, an e-beam is directed

at the target and the kinetic energy of the electrons is transformed to thermal energy upon impact.

The ALE process occurs by gas phase transport of the constituents of a film in alternating sequence to form the desired thin-film on the substrate [16]. This builds up the deposited material one atomic layer at a time. A complex chemistry is involved in this process and accurate deposition conditions are required to ensure stoichiometric deposition of material.

MOCVD refers to a process where the formation of a solid film on a substrate occurs from the reaction of vapor phase metal-organic precursors. In this process the reactant gases are brought into a reaction chamber and are decomposed and reacted at a heated surface to form the thin-film.

The ACTFEL devices used for electrical characterization in this study are summarized in Table 2.1.

**Table 2.1** List of characterized SrS materials.

Deposition Method	Manufacturer	Stack	Deposition Temperature	Anneal Temperature	Ce Doping	Phosphor Thickness
Sputtered	Planar America	Normal	200 °C	750 °C	0.3 mol%	7500 Å
E-beam Evaporation	Westaim, Corp., Canada	Inv.	350 - 400 °C	550 °C	0.2 mol%	11,000 Å
ALE	Planar International, Espoo, Finland	Normal	380 °C	500 °C	0.5 mol%	6700 Å
MOCVD	Los Alamos National Laboratory	Normal	450 °C	Unknown	0.03 mol% (10X under-doped)	5400 Å

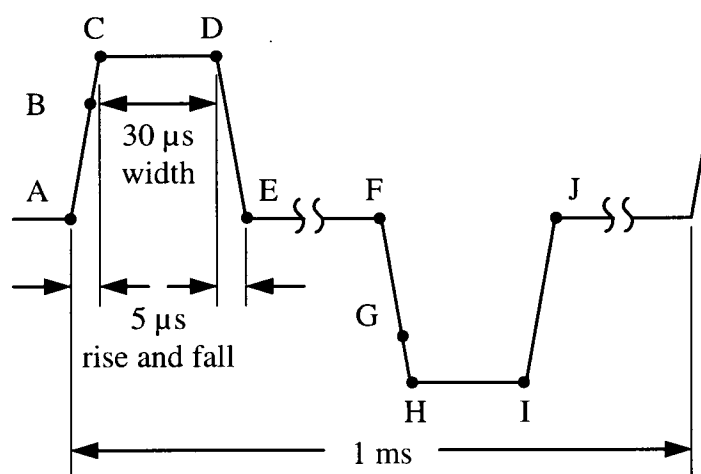


**Figure 2.3** Standard ACTFEL driving waveform.

## 2.4 Device Operation

The operation of an ACTFEL device is governed by the application of an AC driving waveform. ACTFEL researchers have used a variety of driving waveforms: sine wave, triangular waves, and bipolar trapezoidal waves. The waveform used throughout this research is the bipolar trapezoidal waveform. This particular type of waveform has the benefit of distinctly separating the various regions of operation of the ACTFEL device. The correspondence between ACTFEL device operating regions and the driving waveform lends itself to direct manipulation of the driving pulse to fit specific experimental needs.

The general theory of ACTFEL device operation is that when a large external bias is applied, electrons are emitted from the insulator-phosphor interface at the cathodic side. The electrons are then accelerated by the resultant electric field and may strike a luminescent impurity. If the electron has gained enough energy from the electric field, it can transfer sufficient energy to the luminescent impurity to excite it into an excited state. When the excited state of the luminescent impurity relaxes back to its ground state, energy is released in the form of photons. The emission of photons

from excited luminescent impurities is the cause of the luminescence observed in ACTFEL devices. Eventually, the electrons emitted by the cathodic interface drift across the entire polarity with a similar magnitude is applied to the device, the whole process of electron emission, luminescent impurity excitation and relaxation, and electron collection occurs all over again but in the opposite direction.

An alternate way of depicting the operation of an ACTFEL device is to construct a cycle of energy band diagrams, as shown in Fig. 2.4. The cycle is started from a flat-band condition with no external bias applied, as indicated in Fig. 2.4 (a). This corresponds to point A of the driving waveform as shown in Fig. 2.3. When the phosphor electric field reaches some critical value, electrons tunnel out of energy states at the insulator-phosphor interface and into the conduction band of the phosphor host. These energy states are termed interface states and are distributed throughout the band gap. The emitted electrons are accelerated to the opposite interface by the electric field applied across the device. The charge that contributes to this conduction current is known as the conduction charge. These electrons may impact a luminescent impurity as they transit the phosphor and if they have gained enough energy from the field, they will transfer their energy to the impurity and leave it in an excited state. This is shown in Fig. 2.4 (b) and corresponds to point B in Fig. 2.3. The Ce impurities in the SrS host decay quickly, yielding a light pulse that corresponds to this section of the applied waveform and is known as the leading edge light pulse. At point C on the driving waveform, as shown in Fig. 2.3, most of the available electrons have transited the phosphor and have been collected at the opposite interface. The long plateau used in the bipolar trapezoidal waveform, represented by the region between points C and D in Fig. 2.3, allows for any electrons that are still available at the cathodic interface to be emitted from the interface and transit the phosphor. Since the external bias is held constant during this portion of the applied waveform, the charge transfer reduces the internal field across the phosphor. When the externally applied bias is removed, point E in Fig. 2.3 is reached and the condition shown in Fig. 2.4 (c) is obtained.

During the interpulse interval, from point E to point F in Fig. 2.3, there is a non-zero internal field due to the charge imbalance that is setup during the application of the

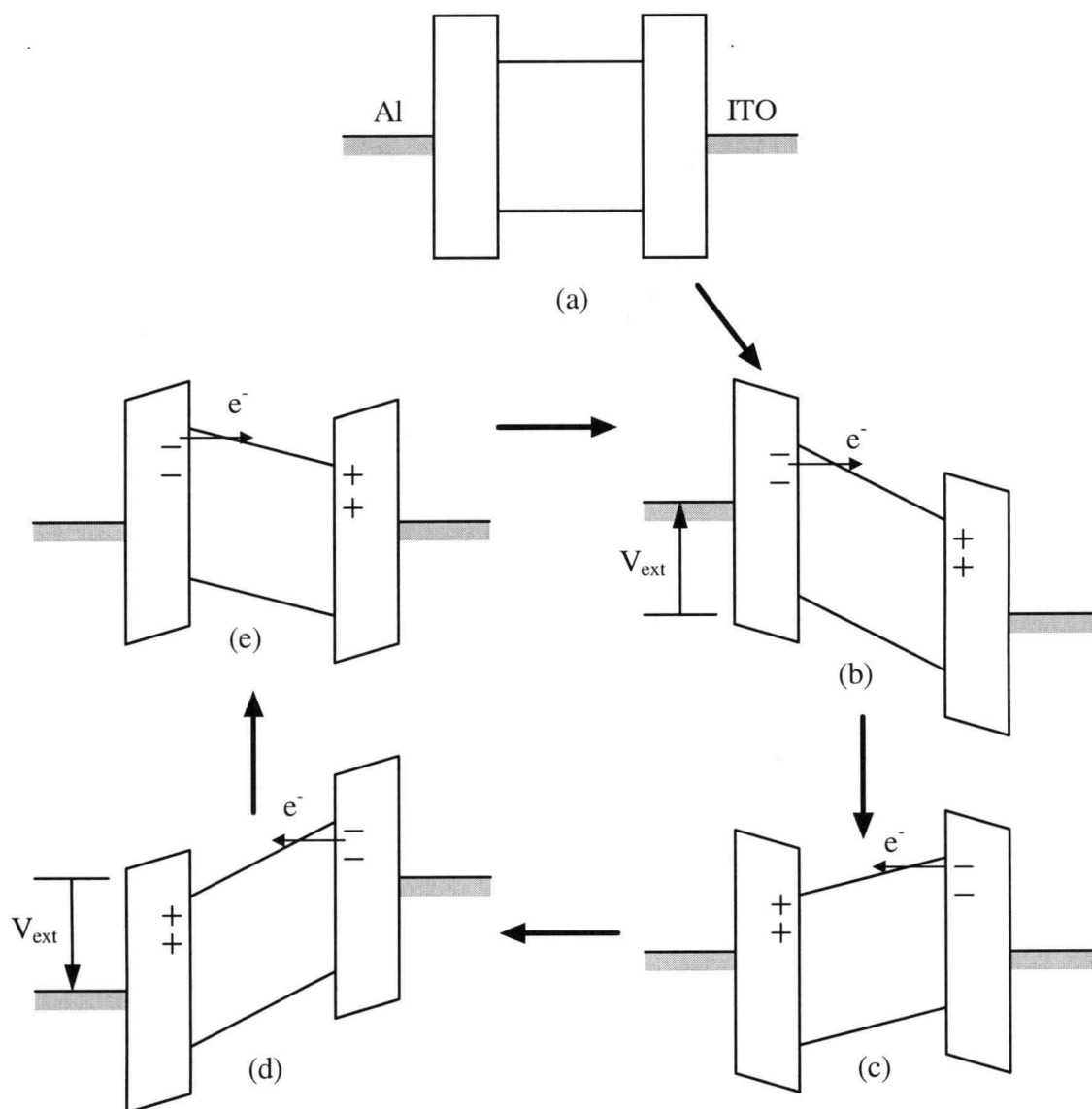


**Figure 2.4** Cycle of energy band diagrams.

external bias. This non-zero field is denoted as the internal polarization field and the excess charge that is collected at the interface is known as the internal polarization charge. Usually this internal polarization field is strong enough to cause emission of some of the electrons from the interface. The charge that is emitted during this zero voltage portion of the driving waveform is termed the internal leakage charge and causes a further reduction in the internal field.

The polarity of the internal polarization field as set up by the polarization charge aids the externally applied bias of the next pulse, i.e. the external bias necessary for the onset of conduction is reduced. This leads to Fig. 2.4 (d) which corresponds to point G in Fig. 2.3. From here the device operation is the same as that for the positive polarity pulse with the exception that the electrons travel in the opposite direction and, thus, Fig. 2.4 (e) shows that the electrons have set up a polarization field similar to that seen in Fig. 2.4 (c) but of opposite polarity. When the next pulse is applied, a reduction of the required externally applied bias for the emission of electrons occurs, just as before.

## 2.5 Dynamic Space Charge in an ACTFEL Device

The above discussion is limited to devices that exhibit no dynamic generation and annihilation of space charge in the phosphor material. Space charge in a SrS:Ce ACTFEL device occurs when impurities in the SrS are ionized, as described in the previous section, or by field emission of an electron from a Ce atom in the lattice [17, 18, 19]. Field emission of a carrier occurs when the excited state of the impurity in the phosphor host is close enough in energy to the conduction band that tunneling of an electron can occur in the presence of an electric field. In either case, the impurity becomes a positively charged entity that is spatially bound to a particular location in the host, hence the term space charge. The space charge that is formed during one polarity of the driving waveform is annihilated during the next polarity pulse. This generation and annihilation of the same space charge for a full cycle leads to the classification of this space charge as dynamic space charge. This dynamic space charge manifests itself as anomalies [20, 21, 22, 23] in the electrical measurements that are not observed in evaporated ZnS:Mn devices having no dynamic space charge. Research has shown that these anomalies are strongly affected by the crystallinity [24, 25, 26] of the host material which implies that native defects in the crystal lattice and the inclusion of Ce in the phosphor result in large amounts of dynamic space charge generation which, strongly effects the electrical characterization and operation of the device [17, 18, 19, 24, 27].

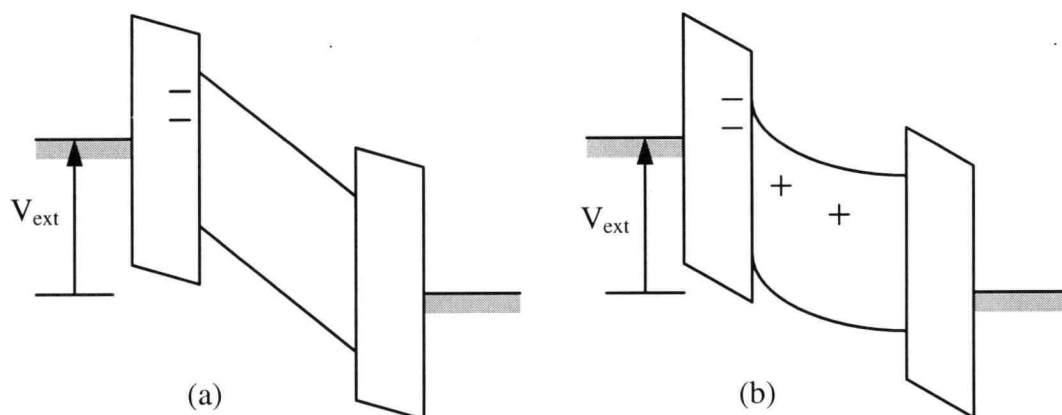


**Figure 2.5** Energy band bending (a) without space charge, and (b) with positive space charge.

Any kind of space charge in the phosphor layer will cause the energy bands to curve and the electric field across the phosphor is no longer a constant, as shown in Fig. 2.5 (b). If positive space charge is assumed to exist in the phosphor, then the field near the interface where electrons are being sourced (i.e. the cathode), is enhanced while the field near the collecting interface (i.e. the anode) is reduced. This field enhancement at the cathode reduces the barrier for electron tunneling and improves carrier injection into the phosphor layer. The field reduction at the anode allows the electron distribution to cool down before hitting the interface which reduces the amount of insulator damage at the interface caused by electrons cooling down via phonon emission. This also reduces the chance of electrons being injected into the insulator layer and becoming trapped. Note that we cannot directly measure fields at the interfaces; only the average field across the phosphor can be measured.

The field distribution caused by space charge in the ACTFEL device is important from a device operation perspective. Field enhancement at the emitting interface translates to a reduced turn-on voltage from what would be observed with no space charge. Field reduction at the collecting interface increases device reliability by extending the useful life of the phosphor-insulator interface. SrS:Ce devices exhibit large amounts of dynamic space charge without which the phosphor would be unsuitable for use in ACTFEL devices. The electrical characteristics that arise from

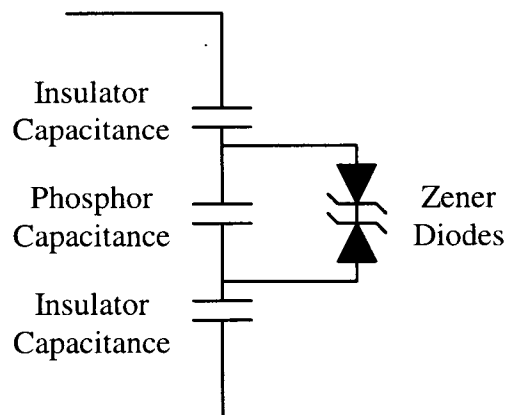


**Figure 2.6** Simple ACTFEL equivalent circuit.

dynamic space charge generation in SrS:Ce ACTFEL devices are further discussed in Chapter 4.

## 2.6 Device Modeling

In this section various levels of device modeling that can be employed to simulate device operation are discussed. The simplest, and therefore the most inaccurate model, is the equivalent SPICE circuit model shown in Fig. 2.6. This model was proposed by Smith [29] and refined by Davidson, et al. [30,31].

The capacitance values for the insulators and the phosphor can be calculated from physical material parameters. These calculated values are referred to in this study as  $C_i^{\text{phys}}$  and  $C_p^{\text{phys}}$ , respectively. The breakdown voltage of the zener diodes is set to match the threshold voltage for the onset of conduction in the phosphor. Davidson's equivalent circuit model was further refined by Douglas [13]. Space charge is not accounted for in any of these earlier circuit models. The modeling effort was taken to a new level with the inclusion of space charge by Keir [32]. Keir develops two very sophisticated models that account for dynamic space charge due to field emission and impact ionization in the ACTFEL device. This modeling effort has allowed researchers to probe the physics of ACTFEL devices that are dominated by dynamic space charge.

The accuracy of these models can be estimated by matching simulation results with actual measurements.

## Chapter 3

### ELECTRICAL EXPERIMENTAL TECHNIQUES

This chapter covers the experimental setup and techniques used to electrically characterize SrS:Ce ACTFEL devices. Electrical analysis techniques include capacitance-voltage (C-V) [30,33], external charge versus external voltage (Q-V) [29,34,13], and internal charge versus phosphor field (Q-F<sub>p</sub>) [35].

#### 3.1 Experimental Setup

The circuit used for electrical characterization of the ACTFEL devices consists of a Wavetek model 395 arbitrary waveform generator, a custom-built bipolar high voltage amplifier, a current-limiting resistor, R<sub>s</sub>, the ACTFEL device under test, and a sense element, as shown in Fig. 3.1. This setup is commonly known as the Sawyer-Tower configuration [36] when a capacitor is used as a sense element for measuring voltages proportional to the charge on the device. The sense element for C-V measurements is a 10 Ω resistor. A 100 μF capacitor is used for Q-F<sub>p</sub> measurements. The waveform applied is a 1 kHz symmetric waveform of bipolar trapezoidal pulses, as shown earlier in Fig. 2.3. The waveforms are sampled and digitized using a Tektronix TDS 420 digital oscilloscope. The digitized data is downloaded to the computer for further manipulation. All of the electrical measurements are taken with the sample in steady-state operation; thus, the history of previous pulses is retained.

#### 3.2 Capacitance-Voltage (C-V) Analysis

The C-V measurement is based on monitoring the current through an ACTFEL device. Typically, this is accomplished by measuring the voltage across a small resistor that is placed in series with the ACTFEL device and obtaining the current using

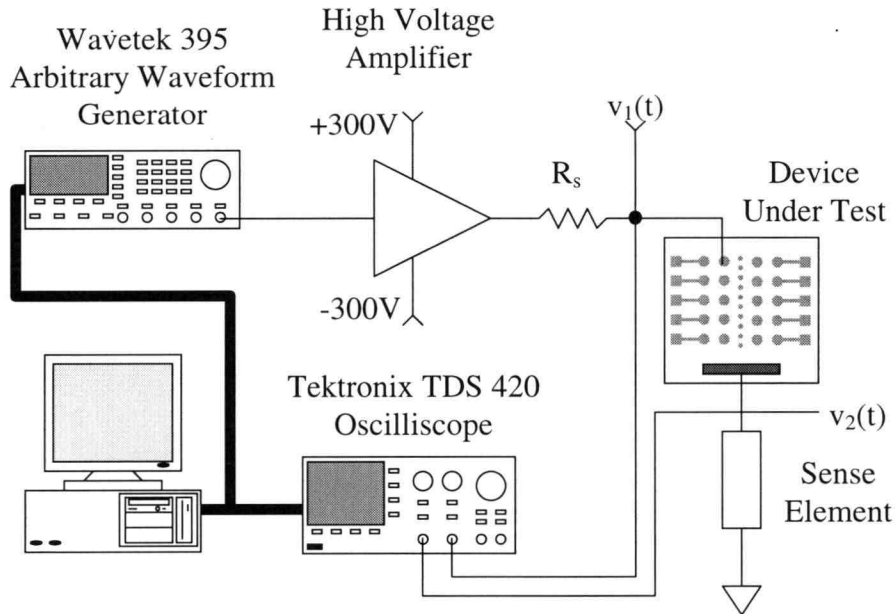


**Figure 3.1** Electrical circuit used to characterize ACTFEL devices.

$$i(t) = \frac{v_2(t)}{R_{\text{sense}}}. \quad (3.1)$$

Then the measured capacitance of the ACTFEL device is determined by the relation,

$$C^{\text{meas}}(V) = \frac{i(t)}{\frac{d}{dt}(v_1(t) - v_2(t))}. \quad (3.2)$$

Alternatively, the measured capacitance can be obtained using a capacitor as a sense element by using the relationship

$$C^{\text{meas}}(V) = \frac{dq(t)}{dv(t)} = \frac{d(C_{\text{sense}} v_2(t))}{d(v_1(t) - v_2(t))}. \quad (3.3)$$

A C-V curve for a typical device that exhibits no dynamic space charge, i.e. almost ideal, is shown in Fig. 3.2. The measured total capacitance,  $C_t$ , and the measured insulator capacitance,  $C_i^{\text{meas}}$ , can be determined from inspection of the C-V curve.  $C_t$  is the capacitance of the ACTFEL stack prior to the onset of conduction in the phosphor.  $C_i^{\text{meas}}$  is the capacitance of the insulators that enclose the phosphor. As

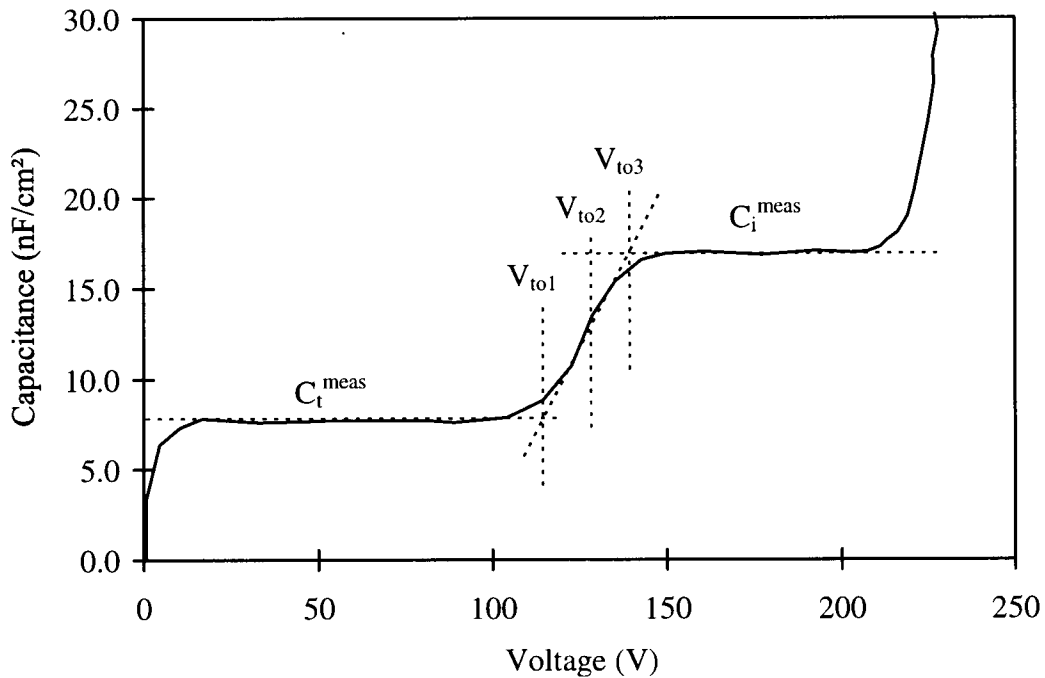


**Figure 3.2** Typical C-V curve for an evaporated ZnS:Mn ACTFEL device with no dynamic space charge.

such,  $C_i^{\text{meas}}$  is an accurate measurement of the physical insulator capacitance only when the conduction within the phosphor is sufficient to completely shunt the phosphor capacitance. The turn-on voltages denoted by  $V_{\text{to1}}$ ,  $V_{\text{to2}}$ , and  $V_{\text{to3}}$ , are the externally applied voltage at which conduction begins to occur, the applied voltage that corresponds to the turn-on voltage as measured by a Q-V curve, and the applied voltage at which the device maintains a steady-state field. The C-V curve has also been used to extract other useful information such as the presence of large parasitic resistances and the pre-clamping density of interface states [30].

### 3.3 External Charge-Voltage (Q-V) Analysis

A Q-V plot is generated by plotting the external charge versus the applied voltage across the EL device, where the external charge is determined from

$$q_{\text{ext}}(t) = C_{\text{sense}} v_2(t). \quad (3.4)$$

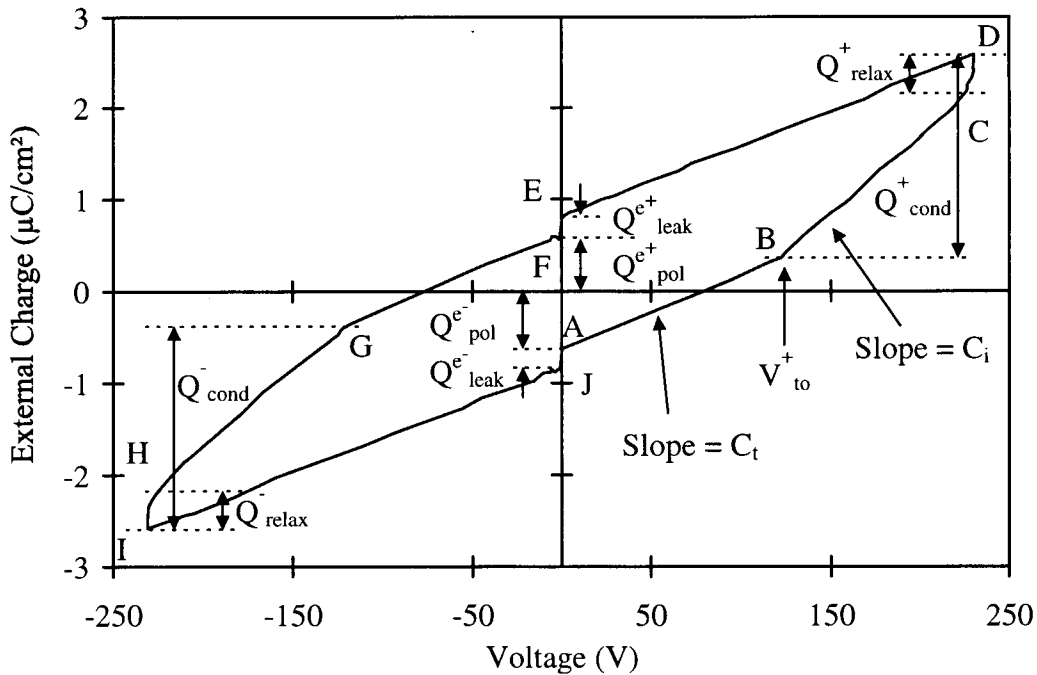


**Figure 3.3** Typical Q-V plot for evaporated ZnS:Mn EL ACTFEL device with no dynamic space charge.

A typical Q-V curve for an evaporated ZnS:Mn ACTFEL device is shown in Fig. 3.3. The labels A through J correspond to critical points of the applied voltage waveform, as given in Fig. 2.3.

A Q-V curve provides several useful quantities. Information regarding various externally measured charge quantities can be read directly from the Q-V curve. Device capacitance in the various operating regimes can be derived from the slope of the Q-V curve according to the relation

$$C = \frac{dQ}{dV} . \quad (3.5)$$

$C_t$  is obtained using the above relation in the region AB.  $C_i$  is found by the same method but using the slope in the region labeled BC. This method of determining the device capacitance has proven to be the most reasonable when constructing Q- $F_p$  curves for devices that exhibit large amounts of dynamic space charge and is the method used in the research presented herein. A more detailed discussion of this method is presented in the next section.

### 3.4 Internal Charge-Phosphor Field (Q-F<sub>p</sub>) Analysis

The Q-F<sub>p</sub> curve uses the same measurement technique and shares the same raw data as that used for the Q-V curve. Analysis of a Q-F<sub>p</sub> plot yields information about conduction charge, polarization charge, leakage charge, relaxation charge, and steady-state field [35, 37], if such a steady state field exists. The internal charge and the phosphor field are computed using

$$q_{\text{int}}(t) = \frac{C_i + C_p}{C_i} q_{\text{ext}}(t) - C_p (v_1(t) - v_2(t)) \quad \text{and} \quad (3.6)$$

$$f_p(t) = \frac{1}{d_p} \left[ \frac{q_{\text{ext}}(t)}{C_i} - (v_1(t) - v_2(t)) \right], \quad (3.7)$$

where  $q_{\text{ext}}(t)$  is the charge measured across  $C_{\text{sense}}$ ,  $v_1(t) - v_2(t)$  is the external voltage measured across the ACTFEL device,  $C_i$  is the total insulator capacitance, and  $C_p$  is the phosphor capacitance. A typical Q-F<sub>p</sub> plot is shown in Fig. 3.4 for an evaporated ZnS:Mn ACTFEL device. Labels A through J correspond to critical points of the

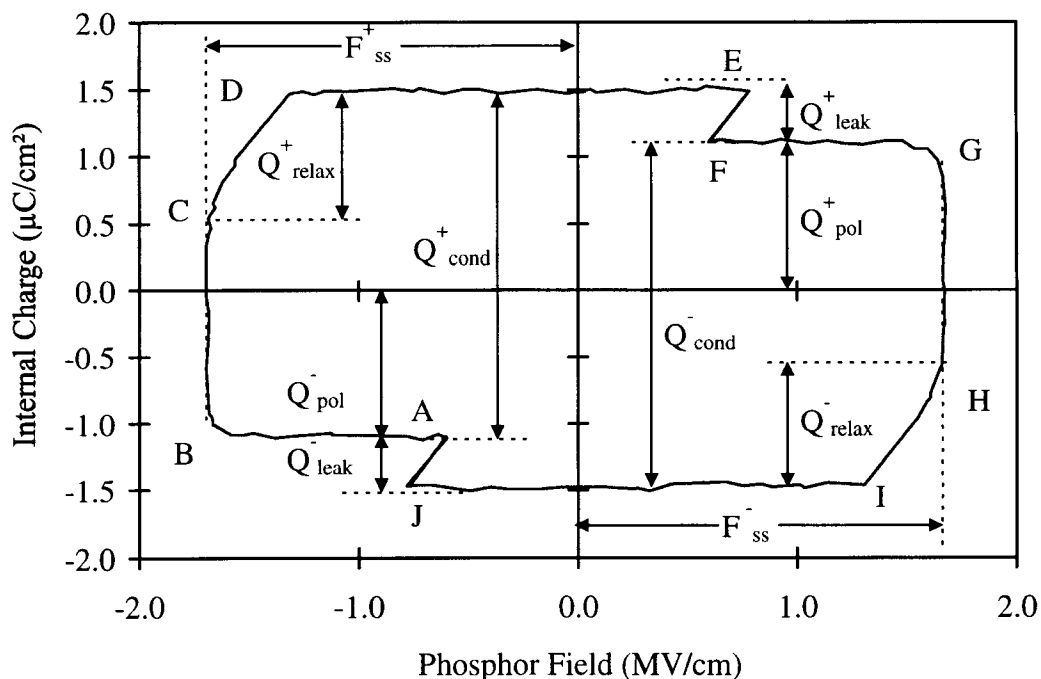


**Figure 3.4** Typical Q-F<sub>p</sub> plot for evaporated ZnS:Mn EL ACTFEL device with no dynamic space charge.

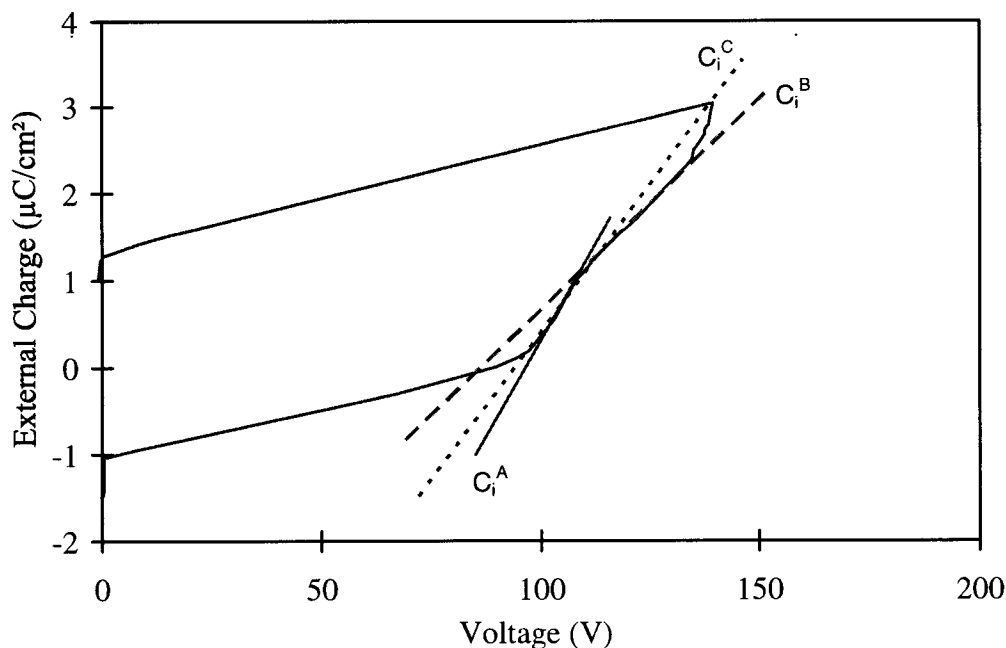


**Figure 3.5** A typical Q-V curve for a SrS:Ce ACTFEL device with dynamic space charge. Only the positive pulse is shown for clarity.

applied voltage waveform, as given in Fig. 2.3.

Equations 3.6 and 3.7 rely on the accuracy of  $C_p$  and  $C_i$  when a Q- $F_p$  curve is constructed. As mentioned previously, the values for  $C_t$  and  $C_i$  which are used to generate Q- $F_p$  curves are taken from the slope of the Q-V curves for the SrS:Ce ACTFEL devices in this study. Figure 3.5 shows a Q-V curve for the positive polarity pulse for a typical SrS:Ce Q-V curve and the measurement locations used to estimate  $C_i$ . Figure 3.6 shows the corresponding Q- $F_p$  curves that are generated using the values of  $C_i$  determined from the Q-V curve. The anomalies in the Q- $F_p$  curves for SrS:Ce are discussed in more detail in the next chapter; these curves are shown here to illustrate subtleties associated with the Q- $F_p$  technique. As shown in Fig. 3.6, the use of  $C_i^{\text{phys}}$  produces a reasonable Q- $F_p$  curve. However, there were several SrS:Ce ACTFEL samples analyzed produced physically unrealistic Q- $F_p$  curves when  $C_i^{\text{phys}}$  is used; field relaxation is so strong in some samples that a reversal of the phosphor field is observed

during the  $V_{\max}$  portion of the driving waveform; such a reversal of the phosphor field seems physically unrealistic.

Note from Fig. 3.6 that the capacitance values,  $C_i^A$  and  $C_i^C$ , produce Q- $F_p$  curves which show an increase in the phosphor field strength in the CD portion of the waveform. This would seem to imply the emptying of more shallow interface and /or bulk states so that a larger field is required across the phosphor in order to emit charge from deeper states. This interpretation seems unlikely, however, since dynamic space charge generation is presumably occurring during this portion of the waveform which would result in a reduction of the average phosphor field in the CD portion of the Q- $F_p$  curve. In contrast, when  $C_i^B$  or  $C_i^{\text{phys}}$  are employed the Q- $F_p$  curves do not exhibit this apparently unphysical increase in phosphor field in the CD portion of the Q- $F_p$  curve. for the SrS:Ce Q- $F_p$  curves presented in this thesis,  $C_i^B$  is used in the Q- $F_p$  equations.

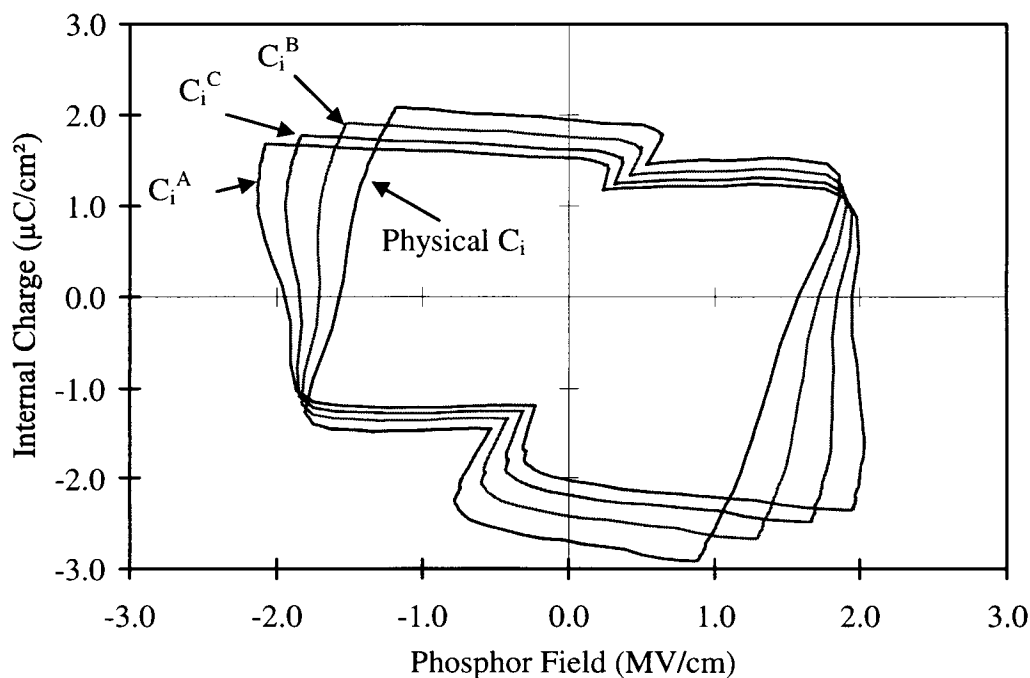


**Figure 3.6** A set of Q- $F_p$  curves for a SrS:Ce ACTFEL device with dynamic space charge using the values of  $C_i$  as determined from the Q-V curve in Fig. 3.5.

Since the accuracy of a Q-F<sub>p</sub> curve depends upon how accurately C<sub>i</sub> is known, it is useful to comment on the trends exhibited in Fig. 3.6. Note in going from C<sub>i</sub><sup>A</sup> to C<sub>i</sub><sup>phys</sup> there is a reduction in the phosphor field in the BD portion of the waveform, an increase in the polarization charge and field, and an increase in the amount of charge collapse. It is important to recognize these trends if the Q-F<sub>p</sub> data presented in this thesis are to be compared to Q-F<sub>p</sub> curves generated using an alternative C<sub>i</sub>.

### 3.5 Experimental Limitations and Sample Preparation

It was observed that practical limitations exist for the equipment used to perform the electrical characterization of ACTFEL devices that exhibit large amounts of space charge.

#### 3.5.1 Effect of Current-Limiting Resistor

It was noted that there exists a correlation between overshoot observed in C-V curves and the value chosen for the current-limiting resistor, denoted as R<sub>s</sub> in Fig. 3.1. A large current-limiting resistance reduces the ability of the amplifier to source and sink current and causes deviations in the applied voltage waveform, as shown in Fig. 3.7.

The effect of R<sub>s</sub> on C-V curves is clearly seen in the pronounced overshoot exhibited in Fig. 3.8. Note that the overshoot increases with increasing resistance. This leads to a desire to use a minimum resistance in the circuit to get the most accurate measurement without catastrophic breakdown of the device. If catastrophic breakdown is prevented only by using an unacceptably large R<sub>s</sub> value, then an alternative procedure is to decrease the slew rate of the applied voltage pulse which reduces the amount of distortion present in the driving waveform. Studies have been performed [38] in which it is concluded that rise/fall times (slew rates) have very little effect on measured ACTFEL device characteristics providing R<sub>s</sub> is not too large.

These overshoot effects can be exacerbated by attempting to drive high-capacitance loads. To alleviate the capacitive loading of the amplifier, samples with

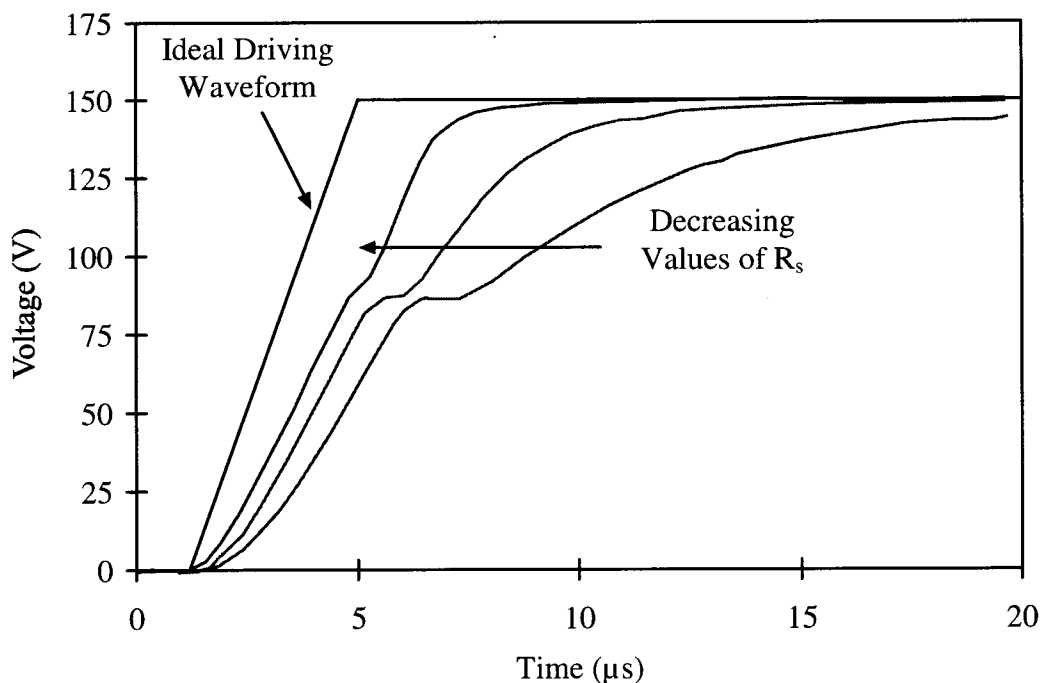


**Figure 3.7**  $V(t)$  showing deviations from an ideal curve as the current-limiting resistance increases.

large device areas (area  $\geq 0.49 \text{ cm}^2$ ) are cut to a standard 2" x 2" size and smaller aluminum contacts (area =  $0.079 \text{ cm}^2$ ) are evaporated onto the plates. This procedure allows reasonable measurements to be taken.

### 3.5.2 Effect of Measured Voltage Offset

The Sawyer-Tower configuration relies on the accuracy of the voltage measured across the sense capacitor that is used to calculate the corresponding charge. If an offset in the measured voltage exists, either on the sense capacitor or across the ACTFEL device, the calculated charge is also offset. This affects both Q-V and Q- $F_p$  curves since the calculation of charge is based on the sensed voltage as per Eqns. 3.4 and 3.6. A Q- $F_p$  curve exhibits a shift in the calculated field as well according to Eqn. 3.7. Most of the SrS:Ce ACTFEL devices studied exhibit an offset voltage. An example of a Q- $F_p$  curve shift due to an offset voltage is given in Fig. 3.9.

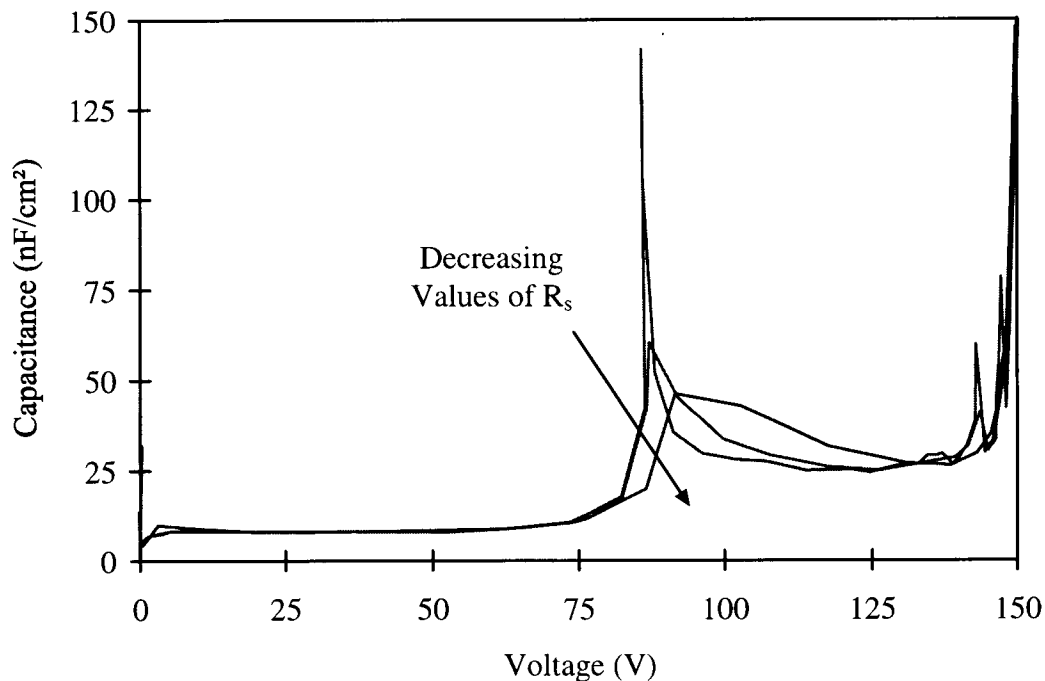


**Figure 3.8** C-V curves showing distortion as a result of the magnitude of the current-limiting resistor.

To correct this offset condition, the signal just prior to the rising edge of the positive and negative pulses is averaged and that quantity is subtracted from the entire waveform to center it about zero. All of the data presented herein have undergone this offset correction.

### 3.6 Dynamic Space Charge Effects

All of the previous discussion deals with devices which do not exhibit dynamic space charge. Consequently, the equations which are presented and used to characterize ACTFEL materials do not take into account dynamic space charge generation.

At present, an alternative to these equations is not available. As mentioned earlier, sophisticated models have been developed by Keir [32] to account for dynamic space charge generation, but these models are best suited for simulation of ACTFEL device operation.

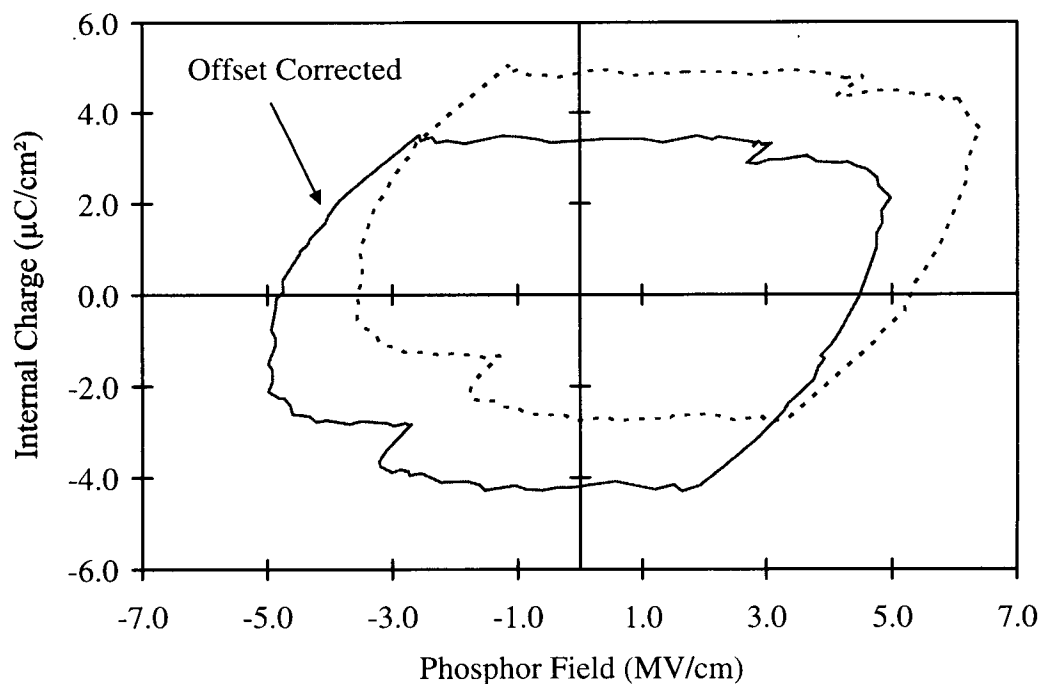


**Figure 3.9** Example of  $Q-F_p$  curve shift due to offset voltage on  $C_s$ .

With this knowledge, that our equations may not be adequate for interpreting data from devices that exhibit dynamic space charge but with no other alternative available for experimental research, one must proceed with caution when interpreting the characteristic electrical curves that are generated. Thus, when the various electrical curves are discussed in the next chapter, most quantities are referred to as average or effective quantities which provide an overall representation of device operation.

## Chapter 4

### ELECTRICAL CHARACTERIZATION OF SrS:Ce DEVICES

Dynamic space charge exhibits itself in the electrical curves that are used to characterize ACTFEL devices as a distortion compared to curves which exhibit no space charge. In particular, space charge induced distortion of SrS:Ce ACTFEL device electrical characteristics are contrasted to the nearly ideal electrical characteristics of evaporated ZnS:Mn ACTFEL devices with sputtered SiON insulators.

#### 4.1 Capacitance - Voltage Experimental Results

A C-V curve for an evaporated ZnS:Mn ACTFEL device with sputtered SiON insulators is shown in Fig. 4.1. This figure shows three curves which are taken with an applied  $V_{\max}$  at approximately 20 V, 40 V, and 60 V above  $V_{\text{th}}$ . ACTFEL devices are

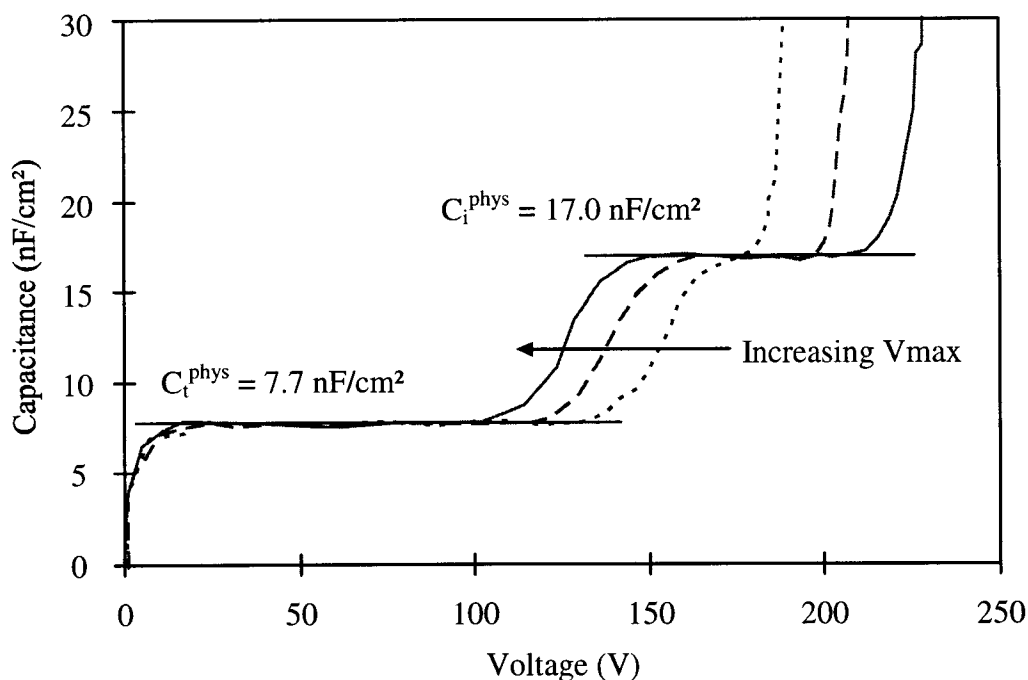


**Figure 4.1** C-V curves for an evaporated ZnS:Mn ACTFEL device with the Al electrode positively biased.

typically operated at  $\sim 40$  V above  $V_{th}$ , where  $V_{th}$  is generally determined from a brightness-voltage (B-V) curve. Subsequent electrical measurements which show three curves are obtained using the same voltage criteria. The curves shown in Fig. 4.1 are with the Al electrode positively biased.

Observe that the measured values of  $C_t$  and  $C_i$  agree with the values calculated from the material constants of the ACTFEL stack and denoted  $C_t^{phys}$  and  $C_i^{phys}$ .  $C_i$  is well defined when  $V_{max}$  is well above threshold, i.e. at  $V_{th} + 40V$  and  $V_{th} + 60V$ . For the case in which  $V_{max}$  is close to  $V_{th}$ ,  $C_i$  is not well defined, as there is not enough conduction current to completely shunt the phosphor capacitance. Also note that there is a rigid shift in the C-V curves to lower voltages as  $V_{max}$  is increased. This is an expected result caused from the build up of polarization charge at the phosphor/insulator interface.

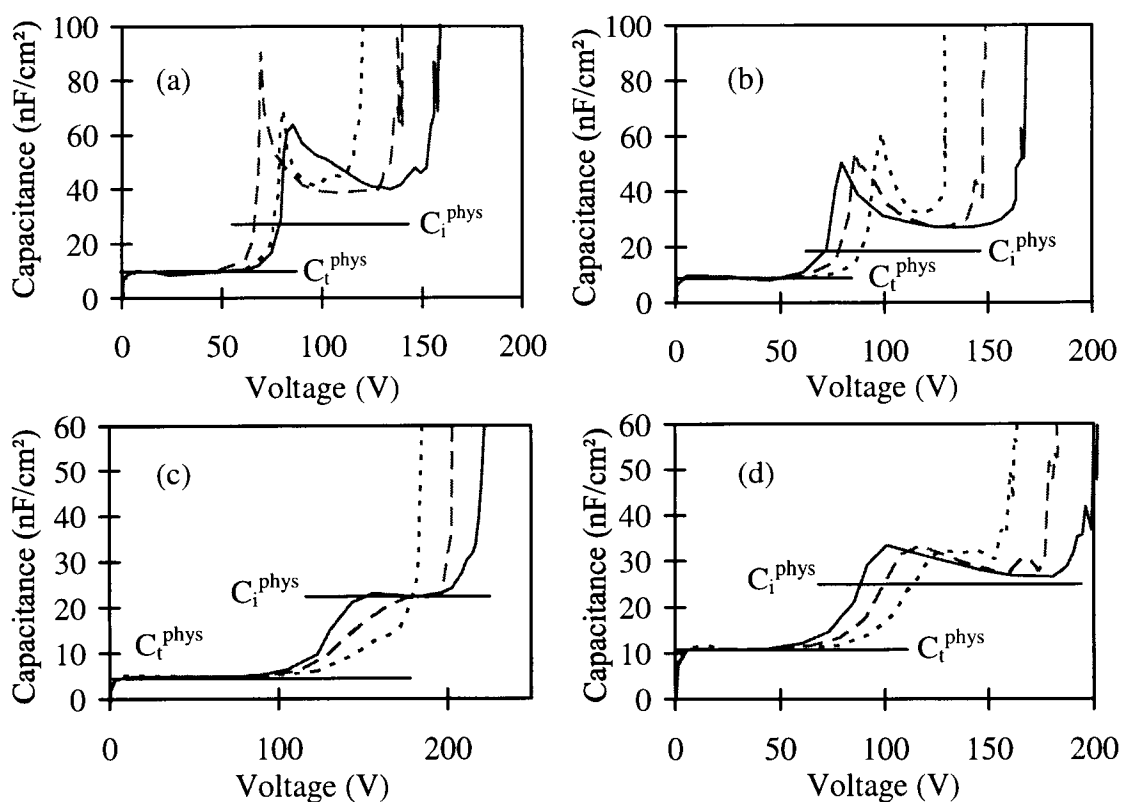


**Figure 4.2** Positive polarity C-V curves for (a) ALE SrS:Ce, (b) sputtered SrS:Ce, (c) e-beam evaporated SrS:Ce, and (d) MOCVD SrS:Ce ACTFEL devices.

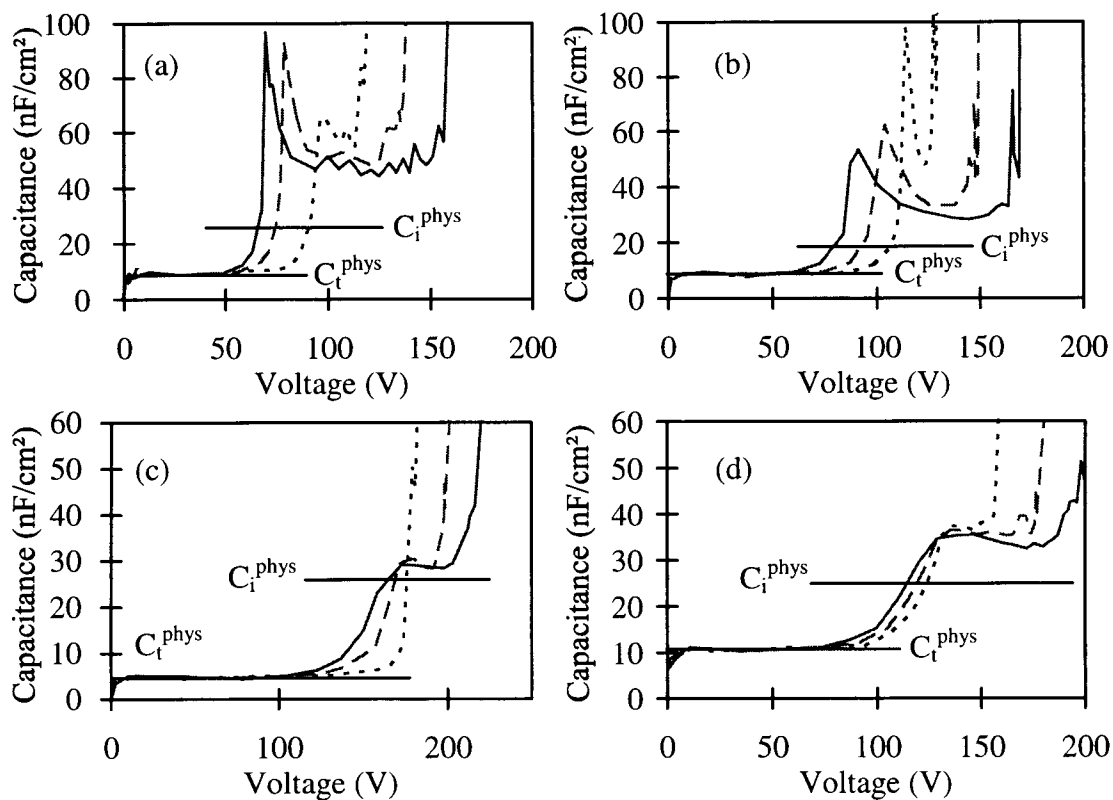


**Figure 4.3** Negative polarity C-V curves for (a) ALE SrS:Ce, (b) sputtered SrS:Ce, (c) e-beam evaporated SrS:Ce, and (d) MOCVD SrS:Ce ACTFEL devices.

A set of positive polarity C-V curves for SrS:Ce ACTFEL devices grown by various methods is shown in Fig. 4.2. A second set of C-V curves is shown in Fig. 4.3 for the same devices biased at a negative polarity. In general, the C-V curves for SrS:Ce ACTFEL devices show some degree of asymmetry with respect to the voltage polarity. This may be due to the use of different insulators to enclose the phosphor at the top and bottom of the phosphor layer. Alternatively, asymmetry may arise from physical or material asymmetries within the phosphor layer.

A comparison of Figs. 4.1 and 4.2 shows significant differences in the C-V characteristics. The most dramatic difference is the overshoot that is present in Fig. 4.2 (a)-(d). This overshoot is attributed to the creation of space charge in the phosphor layer [32] and is an indication that dynamic space charge exists. This overshoot

obscures the measured  $C_i$  such that  $C_i^{\text{meas}}$  is not well defined and is always greater than  $C_i^{\text{phys}}$ . Note that  $C_t^{\text{meas}}$  is well defined and is in close agreement with  $C_t^{\text{phys}}$ . Secondly, Fig. 4.2 shows that  $V_{\text{to}}$  shifts to lower voltages as  $V_{\text{max}}$  increases for curves (b)-(d) while  $V_{\text{to}}$  shifts to a higher voltage for the largest  $V_{\text{max}}$  for curve (a). This phenomenon shown in curve (a) is unique to the ALE SrS:Ce ACTFEL devices tested and occurs for the polarity in which electrons are sourced from the first deposited interface. This is most likely due to Cl migration from the insulator into the phosphor layer. The shift to lower  $V_{\text{to}}$  for curves c and d of Fig. 4.2 show a non-rigid shift that is indicative of carrier emission from bulk states in the phosphor in contrast to exclusively interface state injection, in which case the curves undergo a rigid shift.

Asymmetry in C-V curves caused by interface differences can be seen when comparing Figs. 4.2 and 4.3. Most of the differences are associated with the shift of the turn-on voltage and the slope of the transition from  $C_t$  to  $C_i$ . Of note, curve (a) of Fig. 4.3 shows a definite  $V_{\text{to}}$  shift to lower voltages with an increase in  $V_{\text{max}}$  which is more typical of ACTFEL device operation.

## 4.2 Internal Charge-Phosphor Field (Q-F<sub>p</sub>) Experimental Results

Q-V experiments show results with trends that are similar to those determined from Q-F<sub>p</sub> curves. Some SrS:Ce electrical characteristics are not readily observed in Q-V curves; they are more pronounced in Q-F<sub>p</sub> curves. For this reason, Q-F<sub>p</sub> differences are highlighted. Q-F<sub>p</sub> curves for an evaporated ZnS:Mn ACTFEL device are shown in Fig. 4.4. These curves are used to compare to Q-F<sub>p</sub> curves shown for various SrS:Ce ACTFEL devices in Fig. 4.5.

The first obvious difference between Figs. 4.4 and 4.5 is that field-clamping occurs for the evaporated ZnS:Mn device because the steady-state phosphor field, denoted  $F_{\text{ss}}$ , as determined by the BC portion of the Q-F<sub>p</sub> curve, is constant and independent of  $V_{\text{max}}$ . Field-clamping does not occur for any of the SrS:Ce samples investigated. Indeed, steady-state field operation is never attained, as the BC portion of the curves shown in Fig. 4.5 are never vertical. Note that there is also distinct field

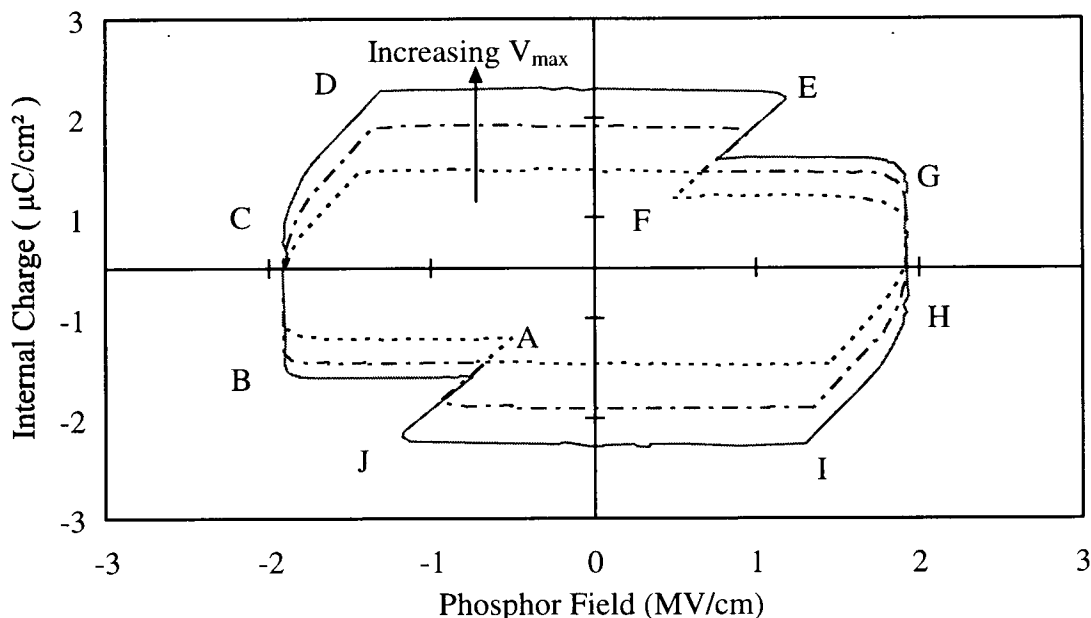


**Figure 4.4** Q- $F_p$  curves for an evaporated ZnS:Mn ACTFEL device.

relaxation between point B and point C which is an indication of dynamic space charge generation in the device. The e-beam evaporated device shown in Fig. 4.5 (c) does not reach steady-state field for the positive voltage polarity during operation but does not exhibit field-clamping. The lack of field-clamping indicates that charge is being sourced from bulk states in the phosphor, as field-clamping occurs when the majority of the charge is sourced from interface states. The second difference between Figs. 4.4 and 4.5, is the charge collapse that sometimes occurs in the DE portion of the Q- $F_p$  curves for SrS:Ce ACTFEL devices. This phenomenon is unique to SrS:Ce devices and is attributed to a collapse of the space charge region. Note that this collapse occurs just when the applied  $V_{max}$  starts to return to zero. This indicates that there is a build-up of carriers at the anode phosphor/insulator interface which are bound in very shallow interface states or are stored at the interface as free carriers by the applied electric field. These characteristics are best explained with the aid of a cycle of energy band diagrams for a SrS:Ce ACTFEL device as shown in Fig. 4.6.

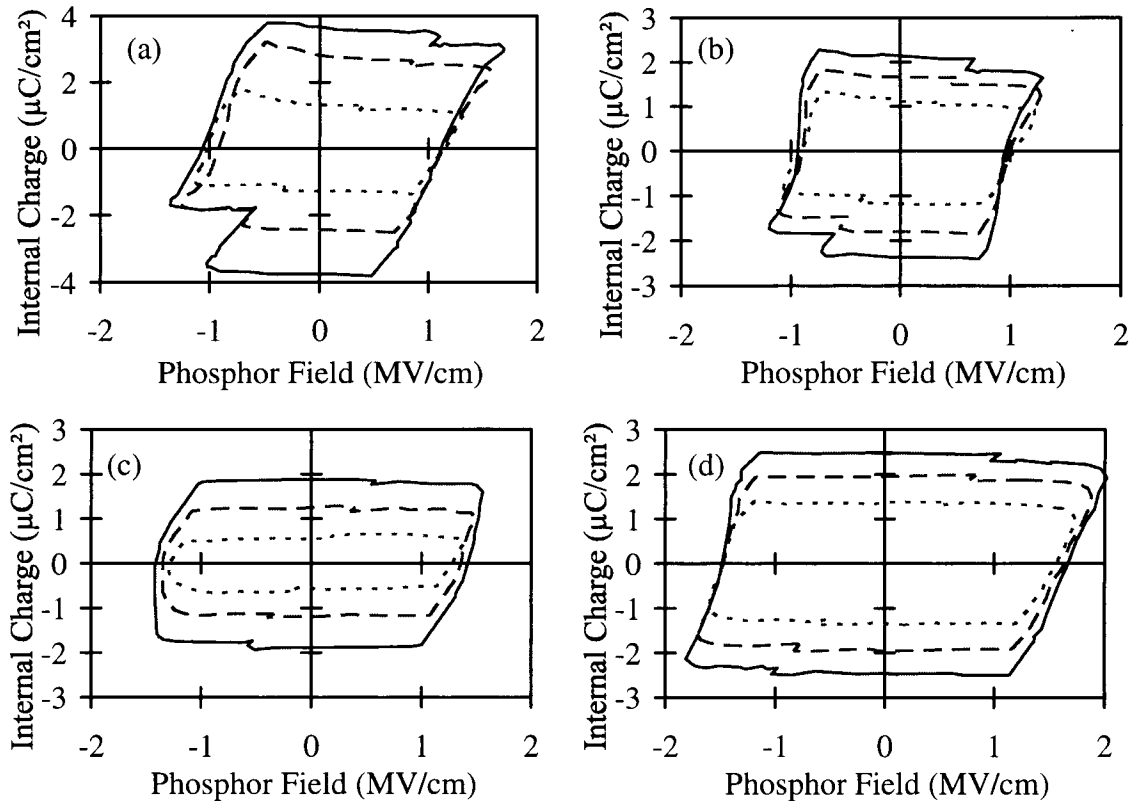


**Figure 4.5** Q- $F_p$  curves for (a) ALE SrS:Ce, (b) sputtered SrS:Ce, (c) e-beam evaporated SrS:Ce, and (d) MOCVD SrS:Ce ACTFEL devices.

Figure 4.6 (a) starts the cycle from a flat band condition with no external bias applied. Figure 4.6 (b) shows the state of the device just prior to turn-on with static space charge present as a result of the previous polarity pulse. The static space charge causes band bending such that the cathodic field is enhanced which further reduces the turn-on voltage compared to what it would be if only interfacial polarization charge is present. The dashed line in Fig. 4.6 (b) gives an indication of the magnitude of the average field that would be measured at point B in the operation of the device. This corresponds to the maximum field,  $F_{\text{peak}}$ , that is measured during this polarity of the applied voltage waveform. Note that this average field is greater than that indicated in Fig. 4.6 (c), which shows the energy bands after turn-on. The average phosphor field, as depicted in Fig. 4.6 (c), is reduced from  $F_{\text{peak}}$  due to the generation of space charge in the phosphor layer. The field reduction represented is consistent with SrS:Ce device

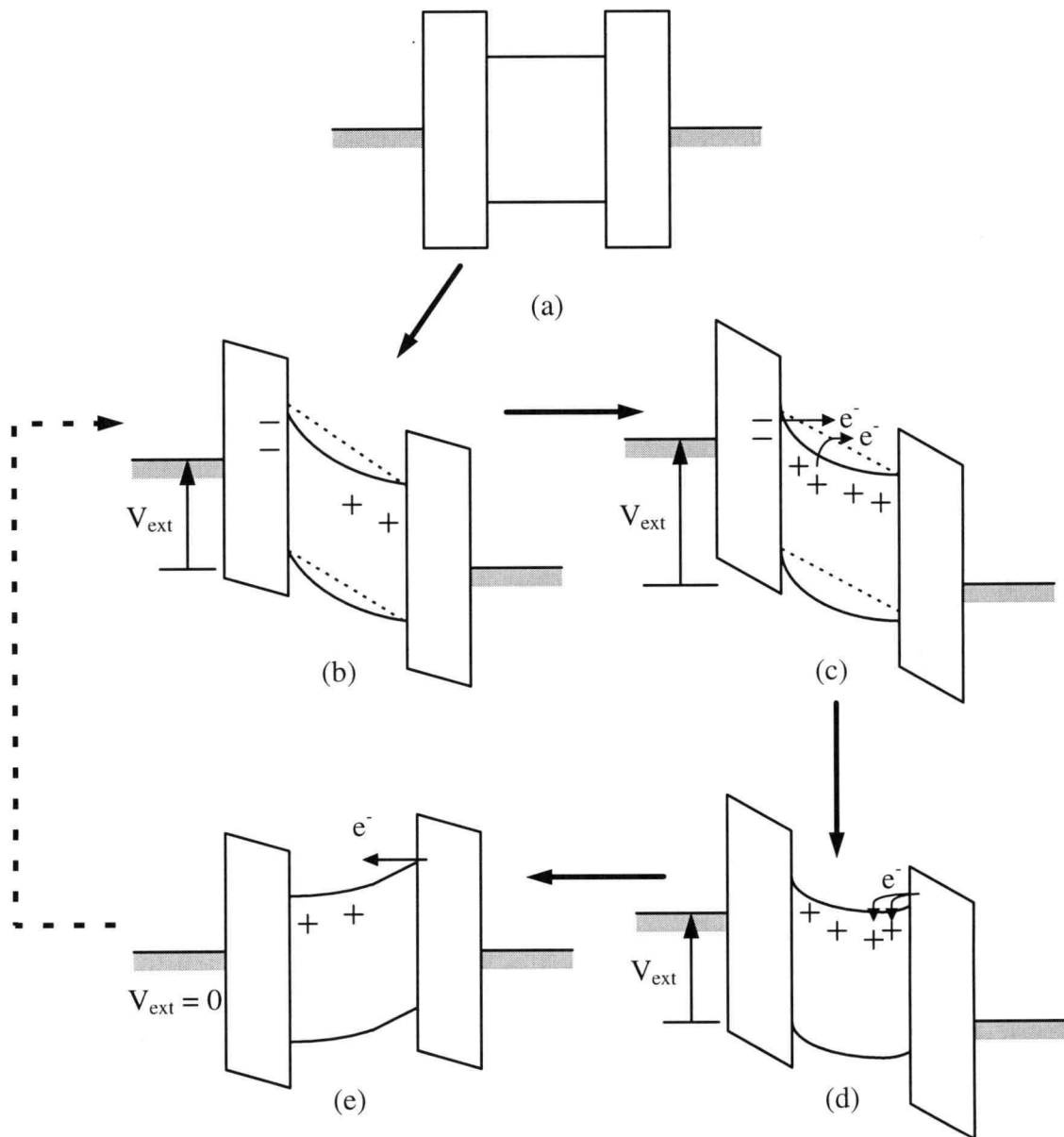


**Figure 4.6** Cycle of energy band diagrams for a SrS:Ce ACTFEL device for a single polarity. The heavy dashed line represents a return to the state depicted in (b) through a similar cycle of energy band diagrams for the opposite polarity pulse.

operation in the region BC. Note also that charge is sourced not only at the interface, but also in states within the bulk of the phosphor. During the CD portion of the driving states either in the phosphor or from the interface as is common to all ACTFEL devices; this is the relaxation charge. Just after point D, where the applied voltage

pulse begins to return to zero, the condition shown in Fig. 4.6 (d) occurs where electrons are sourced from the anodic interface back into the phosphor and annihilate some of the space charge that is present. This is the phenomenon that is referred to as space charge collapse that occurs during the DE portion of the pulse and is unique to SrS:Ce ACTFEL devices. During this transitional stage, the carriers that are either weakly bound in shallow trapping states at the interface or are held near the interface as free carriers, are swept into the phosphor layer and recombine with bulk space charge. The recombination of charge at ionized Ce centers, results in a secondary light pulse that is not present for devices that behave similar to ZnS:Mn. When the applied bias reaches zero, i.e. point E, the condition shown in Fig. 4.6 (e) is reached. There is leakage charge that occurs for SrS:Ce devices in the interpulse interval from point E to F and is similar in nature to that observed for ZnS:Mn devices. A similar set of arguments can be made when the device is in operation subject to the opposite polarity pulse.

Finally, Figs. 4.5 (a) and (b) show asymmetrical leakage charge which can be attributed to differences in the respective interfaces that give rise to deep versus shallow interface states.

### 4.3 Phosphor Field - Thickness Dependence

A strong field dependence on phosphor thickness,  $d_p$ , is noted when  $Q-F_p$  curves for SrS:Ce ACTFEL devices of varying thicknesses are overlaid [42]. The  $Q-F_p$  curves that were used to determine the maximum peak fields were not offset-corrected in the original paper (i.e. Ref. [42]) and therefore do not incorporate the most recent experimental approach. The  $Q-F_p$  curves shown in Fig. 4.7 are offset-corrected and are regarded as giving a more correct understanding of the average fields within the device. Note that for the thinnest device, i.e. the outside curve of Fig. 4.7 (a), the peak field is approximately 5 MV/cm, whereas the thickest device, i.e. the inside curve of Fig. 4.7 (b), shows a peak field of about 1.1 MV/cm. Figure 4.8 graphically shows the phosphor field dependence on phosphor thickness. The phosphor thickness ranges from 1000 Å

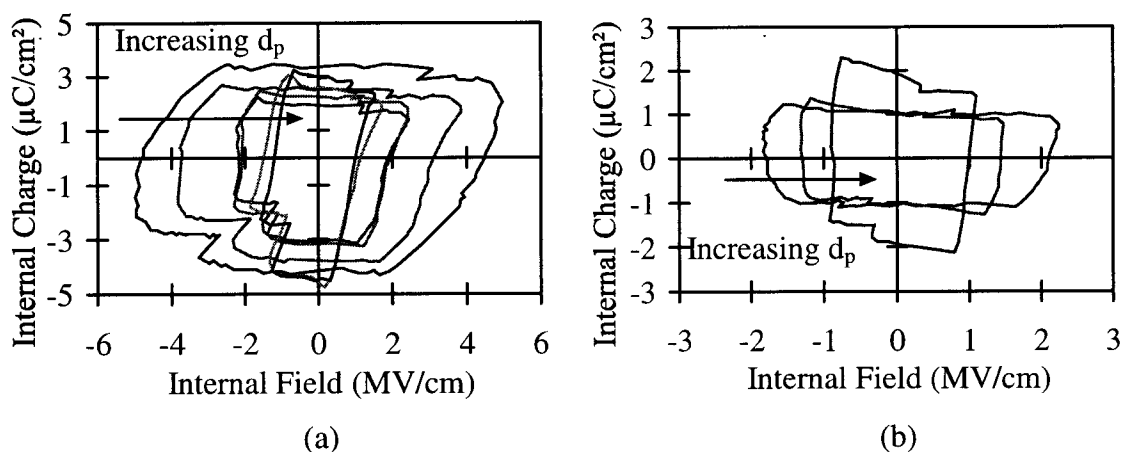


**Figure 4.7**  $Q$ - $F_p$  curves for (a) ALE SrS:Ce and (b) sputtered SrS:Ce ACTFEL devices taken at 60 V over threshold which show the phosphor field dependence on thickness.

to 12,500 Å, as summarized in Table 4.1. Figure 4.7 shows that this trend is similar for both ALE and evaporated SrS:Ce ACTFEL devices indicating that it is independent of the phosphor deposition method employed.

The field dependence noted in Figs. 4.7 (a) and (b) is best illustrated with the use of energy band diagrams. Energy band diagrams consistent with the observation that the threshold voltage remains relatively constant, or increases by a small amount, while the average phosphor field decreases with thickness, as given in Table 4-1, can be constructed and are shown in Fig. 4.9.

The energy band diagrams in Fig. 4.9 are shown for the region of operation corresponding to after turn-on. Figure 4.9 (a) depicts a thin SrS:Ce ACTFEL device while Fig. 4.9 (b) shows a thick SrS:Ce ACTFEL device. At turn-on, dynamic space charge is formed and the fields within the phosphor are enhanced near the cathodic interface and reduced near the anodic interface. The dashed lines in Fig. 4.9 give an indication of the average field that would be measured for these devices assuming the simplest case of uniform space charge distribution across the phosphor layer. As indicated in Fig. 4.9, the average field that would be measured for the thick device is less than that for the thin device.

**Table 4.1** A comparison of  $V_{th}$  and  $F_{peak}$  for SrS:Ce ACTFEL devices with varying thicknesses.

Phosphor Deposition Method	Phosphor Thickness (Å)	Threshold Voltage (V)	Peak Phosphor Field (MV/cm)
ALE	1000	110	4.94
ALE	1600	100	3.82
ALE	2800	97	2.41
ALE	3200	90	2.40
ALE	5100	100	1.70
ALE	6700	104	1.50
Sputtered	2700	80	2.21
Sputtered	6000	85	1.46
Sputtered	12500	110	1.07

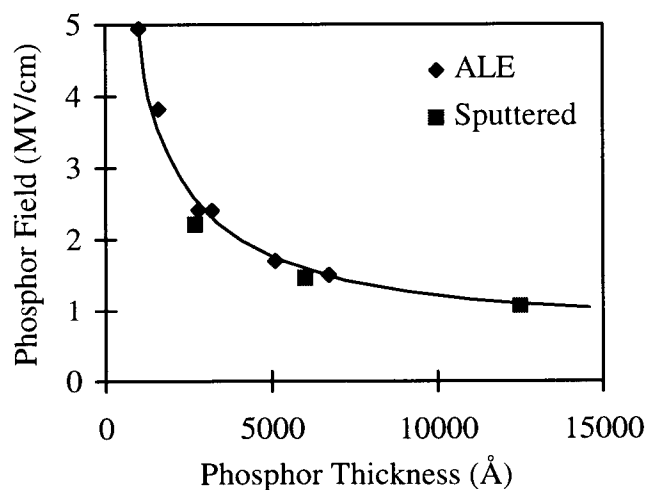


**Figure 4.8** Dependence of phosphor field on thickness based on the values given in Table 4.1.

It has been determined that, for a uniform space-charge distribution, the average phosphor field simply scales with the phosphor thickness [48]. The trend noted in

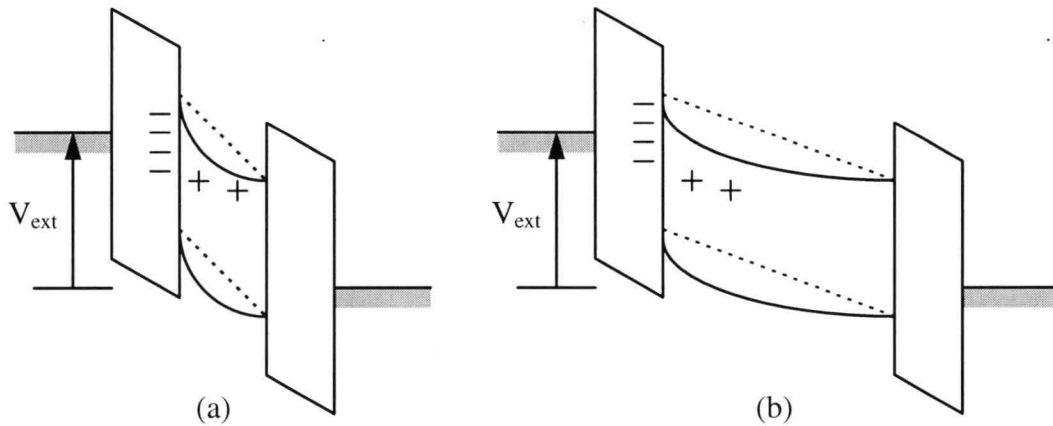


**Figure 4.9** Energy band diagrams for (a) a thin SrS:Ce ACTFEL device and (b) a thick SrS:Ce ACTFEL device.

Table 4.1 is that the average phosphor field drops off quickly but then is relatively independent of phosphor thickness after a certain thickness is attained. This seems to indicate that a non-uniform space-charge region is formed such that a high field region forms near the cathodic interface and, after a certain thickness, is "fully formed" such that the average field is not further reduced for thicker phosphor layers. This is consistent with the field feedback mechanism that is a result of the build up of space charge in the phosphor layer [32].

#### 4.4 Electrical Characteristics of Undoped ALE SrS

Baseline electrical characteristics for a undoped ALE SrS ACTFEL device are determined using  $Q$ - $F_p$  analysis, as shown in Fig. 4.10. The corresponding  $C$ - $V$  curves are not available. It is interesting to note that an undoped ALE SrS ACTFEL device shows a large amount of overshoot which is associated with dynamic space charge creation. The overshoot present in these  $Q$ - $F_p$  characteristics shows that native defects play a significant role in determining the characteristics and operation of ALE SrS:Ce ACTFEL devices. Specifically, the  $Q$ - $F_p$  overshoot present in Fig. 4.10 indicates that dynamic space charge in SrS:Ce ACTFEL devices arises from the ionization of native

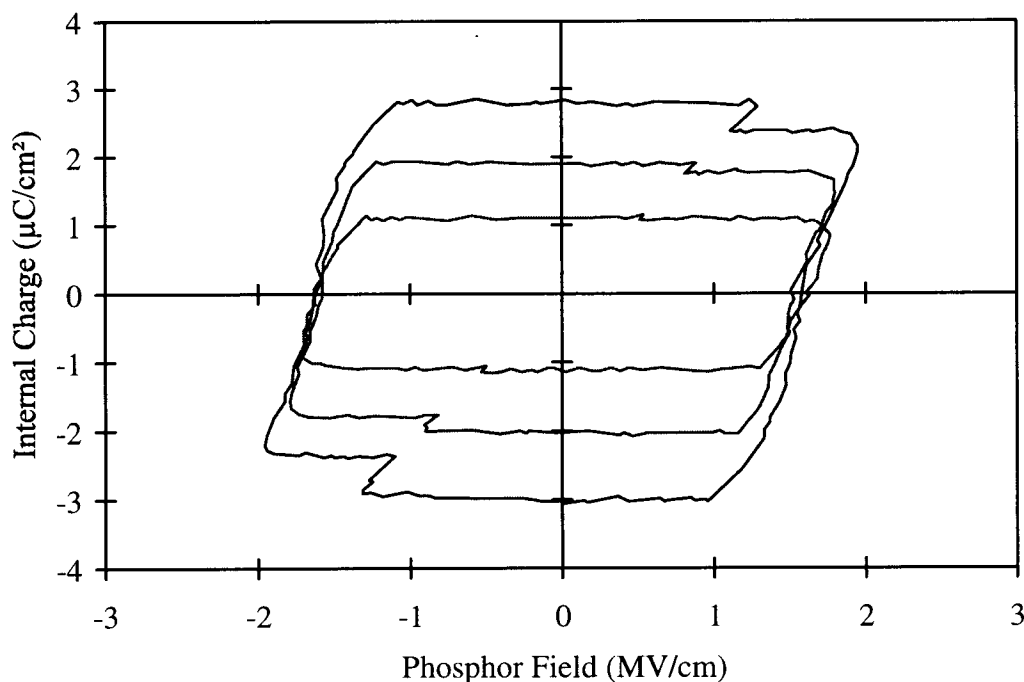


**Figure 4.10**  $Q$ - $F_p$  curves for an undoped ALE SrS sample.

defects as well as Ce luminescent impurities. The nature of these native defects is not yet fully understood. Experiments that characterize various aspects of these traps, such as the transient thermoluminescence (TTL) technique explored in the next chapter, need to be conducted to gain a better understanding of their physical properties.

#### 4.5 Conclusion

The electrical characteristics of an evaporated ZnS:Mn and of several different kinds of SrS:Ce ACTFEL devices are compared and contrasted using C-V and  $Q$ - $F_p$  analysis. Evaporated ZnS:Mn ACTFEL devices exhibit nearly ideal electrical characteristics in which the physics of device operation is relatively well established. In contrast, SrS:Ce ACTFEL devices exhibit characteristics that are not explained by simply invoking the same device physics considerations that apply to ZnS:Mn ACTFEL devices. SrS:Ce ACTFEL device physics are dominated largely by dynamic space

charge effects caused by the ionization of Ce and other trapping states in the host material such as doping-induced strontium vacancies [21].

## Chapter 5

### TRANSIENT THERMOLUMINESCENCE

The exact nature of native defects in SrS:Ce ACTFEL devices is not well established [17, 21, 24]. However, it is recognized that they significantly affect the electrical and optical characteristics of these devices. The transient thermoluminescent (TTL) [43] experiment is used to add to the knowledge of these defects by characterizing their activation energy. Previous TTL work has reported only the activation energy and has been carried out on e-beam evaporated SrS:Ce thin films up to a temperature of 430 K [44]. The work presented in this chapter investigates the response of sputtered and ALE deposited SrS:Ce ACTFEL devices up to temperatures of 560 K and reports the activation energies and capture cross-sections of observed traps. The application of the deep-level transient spectroscopy (DLTS) rate-window concept to the analysis of the luminescent decay curve is presented.

#### 5.1 Introduction

There are several distinct kinds of interactions between deep-level traps and band edges that are possible, as shown in Fig. 5.1. Trapping states, represented by energy levels  $E_{T1}$  and  $E_{T2}$ , can either capture or emit, holes and electrons. For the TTL experiment, it is assumed that the primary concern is with respect to the rate of emission of electrons from traps. The following discussion is restricted to this phenomenon even though there are other possible physical mechanisms that can produce similar results to those observed in a TTL experiment. Some of these possible mechanisms are explored later in the thesis.

Using the principle of detailed balance [47], one can arrive at the well-known equation for the emission rate of an electron from a trap as

$$e_n = v_{th} \sigma_n N_c \exp\left(\frac{-(E_c - E_t)}{k_B T}\right). \quad (5.1)$$

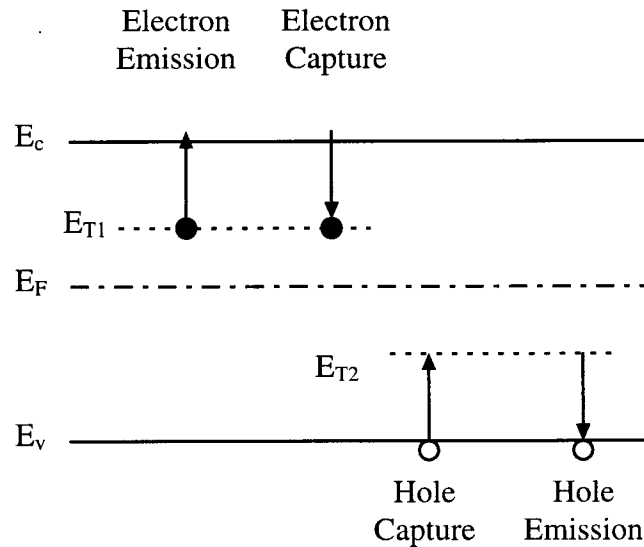


**Figure 5.1** Thermal interactions between traps and band edges.

In this equation,  $v_{th}$  = thermal velocity,  $\sigma_n$  = electron capture cross-section,  $N_c$  = effective conduction band density of states,  $E_c - E_t$  is the trap depth from the conduction band, and  $k_B$  is Boltzmann's constant. The quantity  $E_c - E_t$  is also known as the activation energy and is generally denoted  $E_A$ . Note that this equation shows an exponential dependence of electron emission on both  $T$ , the temperature, and  $E_t$ , the energy of the trap from the conduction band edge. Since  $e_n$  is a rate of emission, the relation,

$$e_n = \frac{1}{\tau_n}, \quad (5.2)$$

can be used to obtain the emission rate from the time it takes for an electron to be emitted from a trap.

The analysis and methodology which follows is that of traditional TTL analysis which is presented in detail in Ref. 43. A summary of that work is presented herein for the readers benefit. Figure 5.2 shows a simplified model of a luminescent material with a single electron trapping state. In this picture,  $G$  is the steady-state generation rate of electron-hole pairs,  $e_n$  and  $c_n$  are the probabilities of electron emission and capture from the trapping state,  $r_{NR}$  and  $r_R$  are, respectively, the non-radiative and radiative

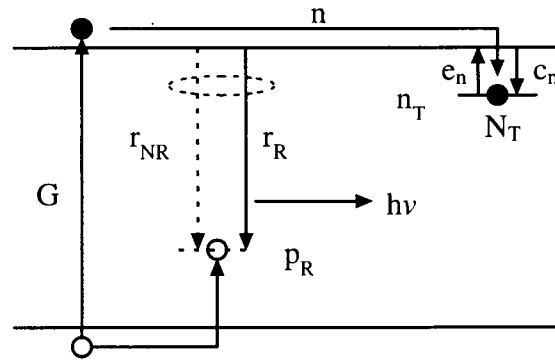


**Figure 5.2** Simplified model of a luminescent material with one electron trapping state.

recombination rates of an electron with a hole at some recombination center,  $N_T$  is the total number of a given trap located near the conduction band edge,  $n_T$  is the number of electrons captured by this trap,  $p_R$  is the number of holes captured at a hole trap located near the valence band (the subscript R indicates that this is the trap at which recombination occurs), and  $n$  is the number of free electrons in the conduction band. By invoking charge neutrality,

$$n = p_R - n_T, \quad (5.3)$$

and thus the rate equations for  $p$  and  $n$  are given by

$$\frac{dn_T}{dt} = -e_n n_T + c_n (p_R - n_T) (N_T - n_T) \text{ and} \quad (5.4)$$

$$\frac{dp_R}{dt} = G - (r_{NR} + r_R) (p_R - n_T) p_R. \quad (5.5)$$

Using the simplified model, as shown in Fig. 5.2, for some steady-state generation of electron-hole pairs,  $G$ , after the system has reached steady-state then  $n^{ss} = p_R - n_T$  and Eqns. 5.4 and 5.5 become

$$\frac{dn_T}{dt} = 0 \Rightarrow e_n n_T = c_n n^{ss} (N_T - n_T) \text{ and} \quad (5.6)$$

$$\begin{aligned} \frac{dp_R}{dt} = 0 &\Rightarrow G = (r_{NR} + r_R)n^{ss}p_R \\ &\Rightarrow n^{ss}p_R = \frac{1}{(r_{NR} + r_R)}G. \end{aligned} \quad (5.7)$$

The luminescence observed at the recombination center is proportional to  $n^{ss}p_R$  such that

$$I_o \propto n^{ss}p_R \Rightarrow I_o = r_R n^{ss}p_R = \frac{r_R}{(r_{NR} + r_R)}G, \quad (5.8)$$

where  $r_R$  is the relevant proportionality constant.

If, at time  $t = 0$ , the steady-state generation of electron-hole pairs is suddenly terminated, i.e.  $G = 0$ , any free electrons in the conduction band will recombine rapidly with trapped holes or be captured by a trap. Equation 5.1 shows that electrons in the trapping states are emitted at a rate determined by the temperature and trap depth and contribute to the observed luminescence if they undergo radiative recombination at the recombination center. This causes a net increase in the observed luminescence at a particular sampling time,  $t_s$ , above that which would be seen without this effect. Concurrently, the number of electrons which are available in the system to recombine at the recombination center decreases to zero and thus the luminescence observed decreases. These two processes, an increase in luminescence as electrons are emitted from traps and a decrease in the number of conduction electrons available for recombination, balance for a particular temperature,  $T_{peak}$ , at a specific sampling time,  $t_s$ , yielding a maximum normalized intensity,  $I_s/I_o$ , at that point. This forms the basis of generating the TTL curves from which the energy of the trap depth can be determined.

For TTL,  $1/t_s$  is substituted for  $e_n$  in Eqn. 5.1, and Eqn. 5.1 is rearranged as

$$E_a = (E_c - E_t) = k_B T \ln(t v_{th} \sigma_n N_c), \quad (5.9)$$

and then put in the form of  $(y_1 - y_2) = m(x_1 - x_2)$ , to arrive at

$$\ln\left(\frac{t_{s1}}{t_{s2}}\right) = \frac{E_a}{k_B} \left( \frac{1}{T_{peak1}} - \frac{1}{T_{peak2}} \right), \quad (5.10)$$

so that when  $\ln(t_s)$  is plotted versus  $1/T_{peak}$ , the activation energy can be obtained as the slope of the line multiplied by  $k_B$ . A semilog activation energy plot of this nature is

known as an Arrhenius plot. Typically, the intercept of an Arrhenius plot yields information regarding the capture cross-section of the trap being analyzed. The capture cross-section, which is related to the intercept, is given as

$$\text{Intercept} = \ln\left(\frac{1}{v_{\text{th}}\sigma_n N_c}\right). \quad (5.11)$$

Note that the intercept value determined from the semilog plot is highly sensitive to the slope, i.e. a small variance in the slope causes a large variance in the intercept. This can lead to a large experimental uncertainty in the capture cross-section. The values for  $v_{\text{th}}$  and  $N_c$  used in Eqn. 5.11 are calculated as

$$v_{\text{th}} = \sqrt{\frac{3k_B T}{m_e^*}} \quad \text{and} \quad (5.12)$$

$$N_c = 2\left(\frac{2\pi m_e^* k_B T}{h^2}\right)^{3/2}. \quad (5.13)$$

The longitudinal and transverse electron effective masses at the X-point conduction band minimum for SrS have been estimated to be 1.4 and 0.4 respectively [50]. This yields a density of states electron relative effective mass equal to 1.26. The numerical values for  $v_{\text{th}}$  and  $N_c$  are calculated at  $T = 300$  K.

The traditional TTL analysis of the luminescent decay curve is based on the thermoluminescent (TL) technique [45,46] and a level of confidence has been established based on correlation between TTL results and previously published TL results as reported in Ref. 44.

There may be other physical mechanisms which produce similar TTL signals. In particular, hole emission from a trap to the valence band and subsequent radiative recombination with a trapped electron could give a similar TTL response. Additionally, it is possible to observe a similar TTL response if the defect at which the electron and hole recombine, can resonantly transfer its recombination energy to the center that is emitting the observed radiation. Note the recombination trap shown in Fig. 5.2, from which the TTL signal arises, could be due to a native trap, a luminescent impurity, an unintentionally incorporated impurity, or even a free hole (if free holes are present).

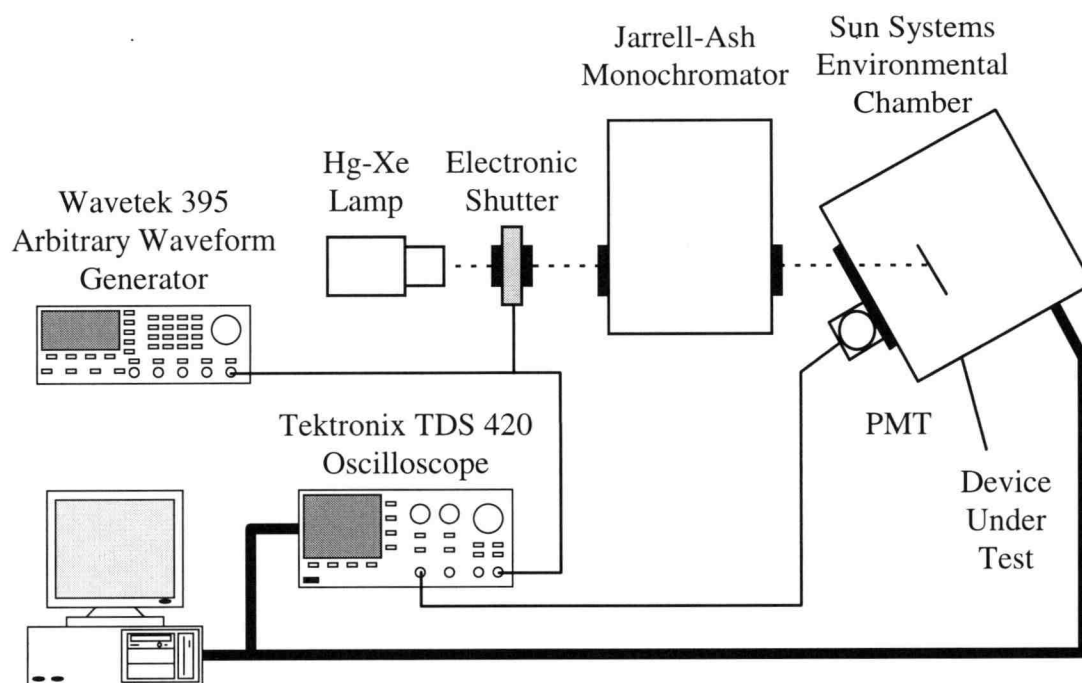


**Figure 5.3** Basic TTL experimental setup.

## 5.2 Transient Thermoluminescence Experimental Setup

The TTL experiment setup is shown in Fig. 5.3. The excitation source is a 75 W Hg-Xe discharge lamp. Light passes through an electronic shutter and is then filtered through a monochromator centered at 250 nm (4.96 eV) and directed onto the sample in the environmental chamber. Light emitted from the sample is transmitted through a high-pass filter to cutoff any signal from the excitation source and is fed to a photo-multiplier tube (PMT). The signal from the PMT is captured by a Tektronix TDS 420 digitizing oscilloscope and is downloaded to the computer for later analysis. A Wavetek Arbitrary Waveform Generator Model 395 is used as a pulse generator to create a 0.5 Hz square wave trigger for the electronic shutter and the oscilloscope. The Sun Systems Model EC-1A environmental chamber is controlled by the computer to increment with a 2 K step between temperature readings and maintain a constant temperature while the signal from the PMT is digitized and downloaded to the

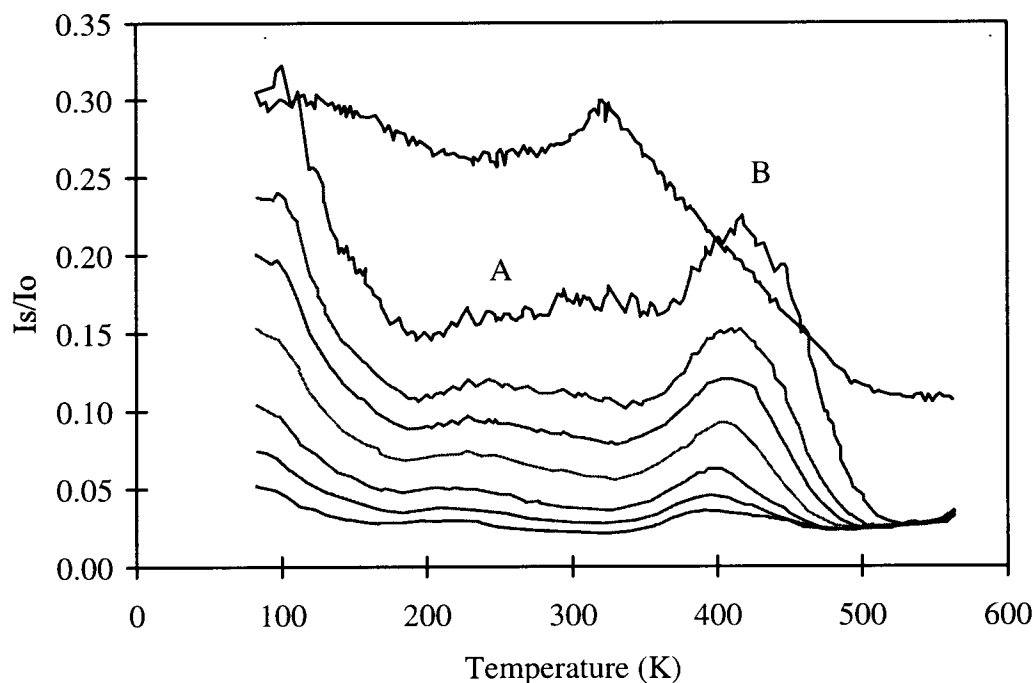


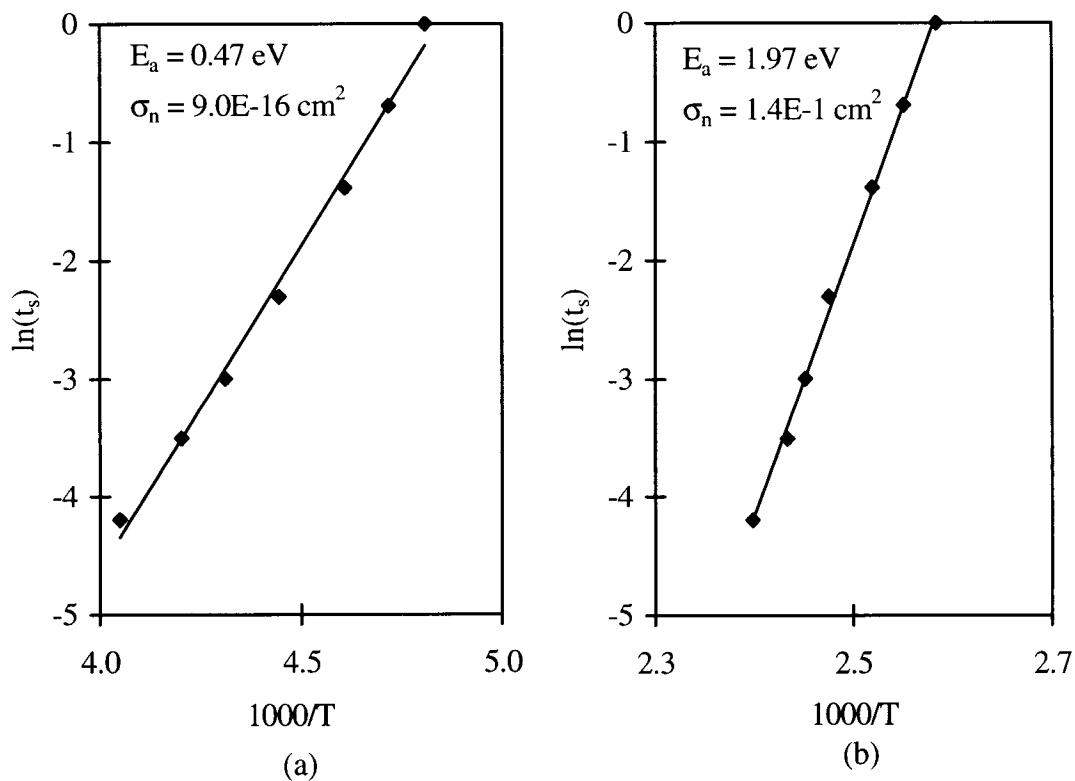
**Figure 5.4** TTL response curves for an undoped, (i.e. no Ce) sputtered SrS ACTFEL device which is doped with Ga. The curves from bottom to top are for sampling time  $t_s = 999$  ms, 500 ms, 250ms, 100 ms, 50 ms, 30 ms, and 15 ms. The top most curve is the steady-state luminescence  $I_0$ .

computer. The environmental chamber uses feedback from a thermocouple attached to the sample to maintain a constant temperature.

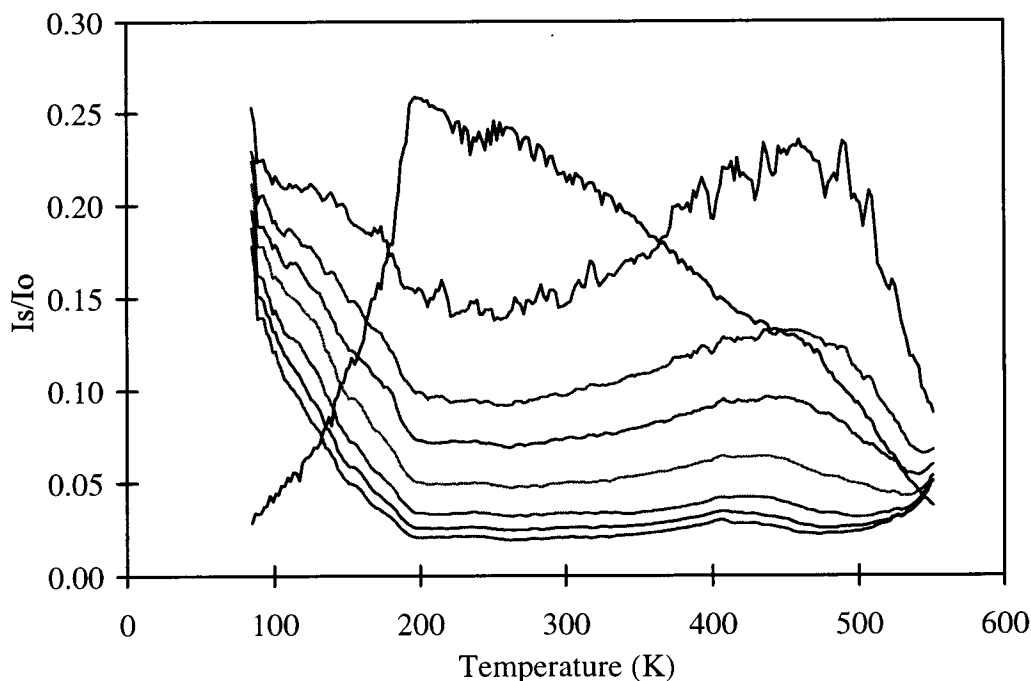
### 5.3 Transient Thermoluminescence Experimental Results

Figure 5.4 shows a set of TTL response curves for an undoped (i.e. no Ce), sputtered SrS ACTFEL device which is doped with Ga. To obtain the activation energy of the traps corresponding to the various peaks and shoulders in Fig. 5.4 requires construction of an Arrhenius plot, which is shown in Fig. 5.5, for the peaks labeled A and B in Fig. 5.4. Data around the temperature peak was greatly expanded so that the temperature at which the peak occurs could be estimated more accurately.

The peak labeled as A and centered at about 250 K, shows an activation energy of 0.47 eV and a capture cross-section of  $9.0 \times 10^{-16} \text{ cm}^2$ . The magnitude of the capture cross-section suggests that this is a neutral trapping state. This peak appears to be associated with the Ce dopant, as hypothesized in previous TTL literature [44]. If this identification is true, then this would indicate that the sample has some residual Ce doping. It was learned that the sputter chamber used to fabricate this sample was also used to sputter SrS:Ce samples just prior to this undoped run and was not cleaned between experimental runs. Residual Ce incorporation in the SrS could account for the weak response seen in the experimental data shown in Fig. 5.4 and identified as peak A. It is also possible that this energy is associated with either a hole trap or an electron trap located 0.47 eV away from one of the band edges; this experiment cannot distinguish between an electron or hole trap.



**Figure 5.5** Arrhenius plots of the peaks seen in the TTL response curves from Fig. 5.4 for the peaks occurring at (a) 250 K and (b) 400 K.



**Figure 5.6** TTL response curves for an ALE SrS:Ce ACTFEL device. The curves from bottom to top are for sampling time  $t_s = 999$  ms, 500 ms, 250ms, 100 ms, 50 ms, 30 ms, and 15 ms. The top most curve is the steady-state luminescence  $I_0$ .

Peak B, occurring at 400 K, yields an activation energy of 1.97 eV and a capture cross-section of  $1.4 \times 10^{-1} \text{ cm}^2$ . The capture cross-section calculated for this peak is unrealistically large and may be related to the sensitivity of the intercept value to the slope of the Arrhenius plot and the uncertainty in the peak data. The exact nature of the defect that is responsible for this peak is not known at this time and has not been previously reported in the literature. The peak may be due to Ga, which is used as a co-dopant for this type of phosphor deposition and, thus, would not have been reported in previously published literature or it may be due to native defects within the phosphor material. It may even be a hole trap. To date, there is no published literature detailing the effective mass of holes for this material; the activation energy and capture cross-section cannot be estimated for this peak with a hole analysis. Further TTL studies are necessary to determine whether this peak is due to Ga by using a similarly grown

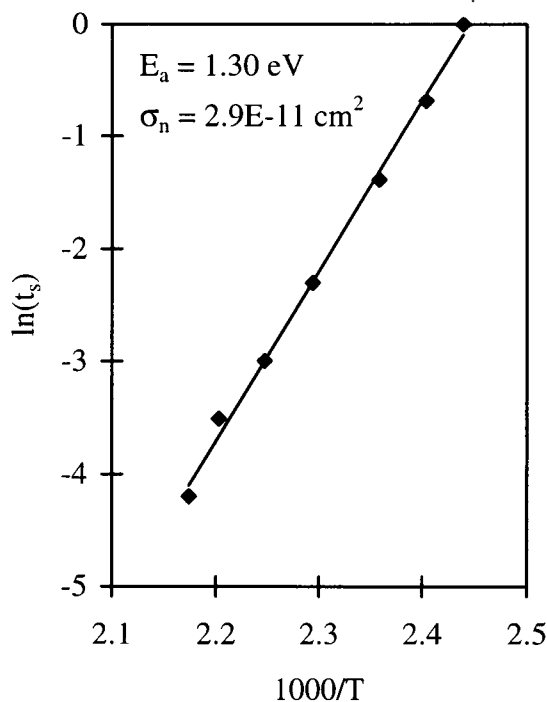


**Figure 5.7** Arrhenius plot of the peak seen in the TTL response curves from Fig. 5.6 occurring at 450 K.

sample without Ga co-doping. This may also be an artifact generated from within the system.

A set of TTL curves similar to those shown in Fig. 5.4 is obtained for an ALE SrS:Ce ACTFEL device and is presented in Fig. 5.6. There is only one dominant peak present for this sample, which occurs at about 450 K. The corresponding Arrhenius analysis of this peak yields an activation energy of 1.30 eV and a capture cross-section of  $2.9 \times 10^{-11} \text{ cm}^2$ , as shown in Fig. 5.7. This peak may be due to native defects in the phosphor. Interpretation of this data is obscured by the fact that a full ACTFEL stack is used in this experiment, thus, the TTL response observed may arise from the material employed as the top insulator. Note the sharp roll-off in the intensity of  $I_0$  at low temperatures for Fig 5.6. This causes an anomaly to be found in the lower temperature range of the normalized curves as  $I_0$  is artificially depressed. The roll-off of  $I_0$  at low temperatures for this particular experiment is due to the formation of ice crystals on the

quartz window of the environmental chamber. To date, the PMT is mounted directly next to the quartz window of the environmental chamber and thus the TTL signals measured are directly affected by complications arising from temperature variations of the chamber windows. These complications can be alleviated by keeping the quartz window and PMT fixture at a reasonable temperature or by mounting the PMT in a fixture that is physically separated from the environmental chamber so that the temperature of the chamber and the PMT can be separately controlled. This experimental modification will yield more reliable results for low temperature peaks. The steady decrease of  $I_0$  at higher temperatures may be due to increased phonon interaction with the recombination center causing a larger percentage of the electron-hole recombination to be non-radiative, i.e. thermal quenching. Using the normalized intensity corrects for this variation.

#### 5.4 Rate-Window Analysis of the Luminescent Decay Curves

The traditional TTL analysis of the luminescent decay curves sometimes yield unsatisfying results, as demonstrated by the unrealistically large capture cross-section of peak B in Fig. 5.4. This result in particular caused considerable concern over the validity of the results obtained using traditional TTL analysis. The use of DLTS-like rate window analysis is proposed as an alternative for characterizing the observed traps. The DLTS principles and methodology are examined in great detail in Ref. 49. The key equations are summarized herein. The basis for the DLTS rate-window concept is the emission rate of carriers from a trapping state and is given in Eqn. 5.1. Like the TTL analysis, it is assumed that the trap interaction of greatest interest is electron emission. The use of rate-window analysis allows for precise definition of the electron emission rate corresponding to the maximum of a trap peak as

$$e_n^{-1} = \tau_{\max} = \frac{t_1 - t_2}{\ln(t_1/t_2)}. \quad (5.14)$$

where  $t_1$  and  $t_2$  correspond to the sampling times which define the rate-window. The temperature corresponding to the peak maximum, in conjunction with the emission rate,

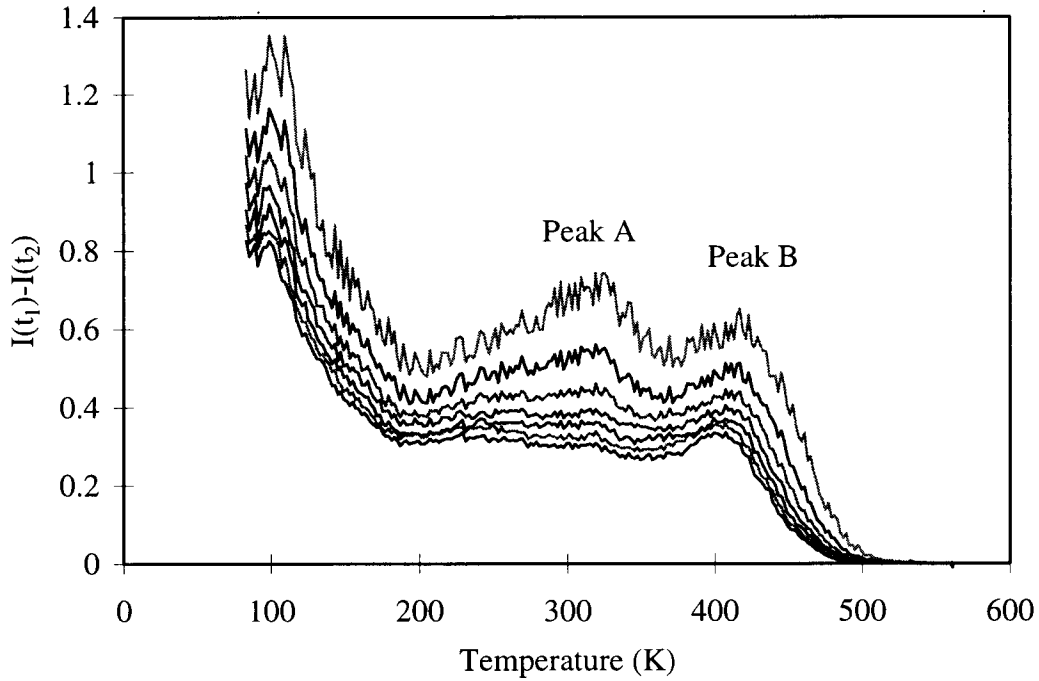


**Figure 5.8** Rate-window curves for an undoped sputtered SrS with Ga codoping ACTFEL device. These curves were constructed using a constant  $t_1:t_2$  ratio of 1:10. The curves from top to bottom are for  $t_1:t_2$  times of 10:100, 20:200, 30:300, 40:400, 50:500, 60:600, 70:700.

can be used to construct an Arrhenius plot where the slope is related to the activation energy by

$$\ln\left(\frac{e_{n1}}{e_{n2}}\right) = -\frac{E_a}{k_B} \left( \frac{1}{T_{\text{peak1}}} - \frac{1}{T_{\text{peak2}}} \right) \Rightarrow |E_a| = |k_B \times \text{slope}|, \quad (5.15)$$

and the capture cross-section can be determined from the intercept as

$$\text{Intercept} = \ln(v_{\text{th}} \sigma_n N_c) \Rightarrow \sigma_n = \frac{\exp(\text{Intercept})}{v_{\text{th}} N_c}. \quad (5.16)$$

This type of analysis does not depend upon the rate at which the temperature is varied so that the same data set used for TTL analysis, which is also temperature ramp rate independent, can be used directly for both types of analysis.

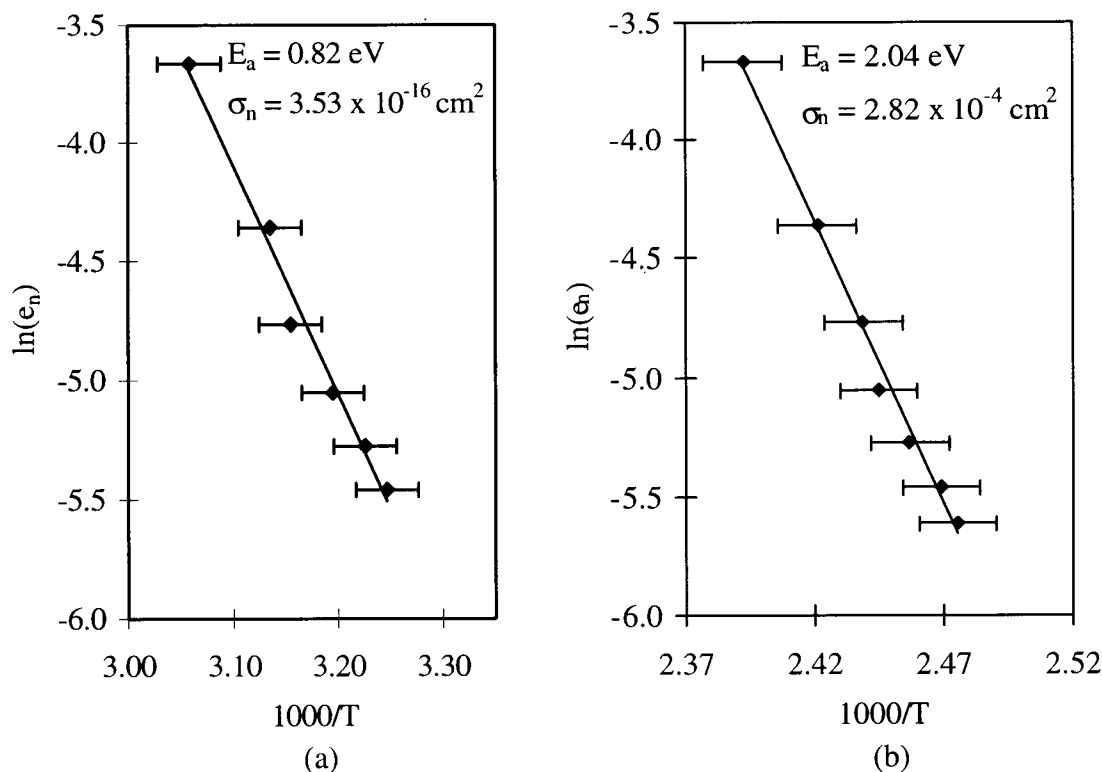


**Figure 5.9** Arrhenius plots of the peaks seen in the rate-window curves from Fig. 5.8 for the peaks occurring at (a) 300 K and (b) 425 K.

The rate-window curves for the undoped sputtered SrS ACTFEL device which is doped with Ga are shown in Fig. 5.8. These curves show two distinct peaks similar in position to those found using the traditional TTL analysis. The large amount of noise present when analyzing this data using the DLTS rate-window approach is due to the lack of signal averaging; this leads to potential experimental errors. Arrhenius plots of the peaks shown in Fig. 5.8 are constructed and shown in Fig. 5.9. The Arrhenius analysis of the peak labeled A in Fig. 5.8 yields an activation energy of 0.82 eV and a capture cross-section of  $3.53 \times 10^{-16} \text{ cm}^2$ , as shown in Fig. 5.9(a). It is possible to resolve the peak temperature only for the first 6 curves, i.e. from the 10:100 curve to the 60:600 curve. The activation energy determined using this method is somewhat higher than that value of 0.47 eV determined from TTL analysis. The capture cross-section is the same order of magnitude as that found from TTL. The difference in activation

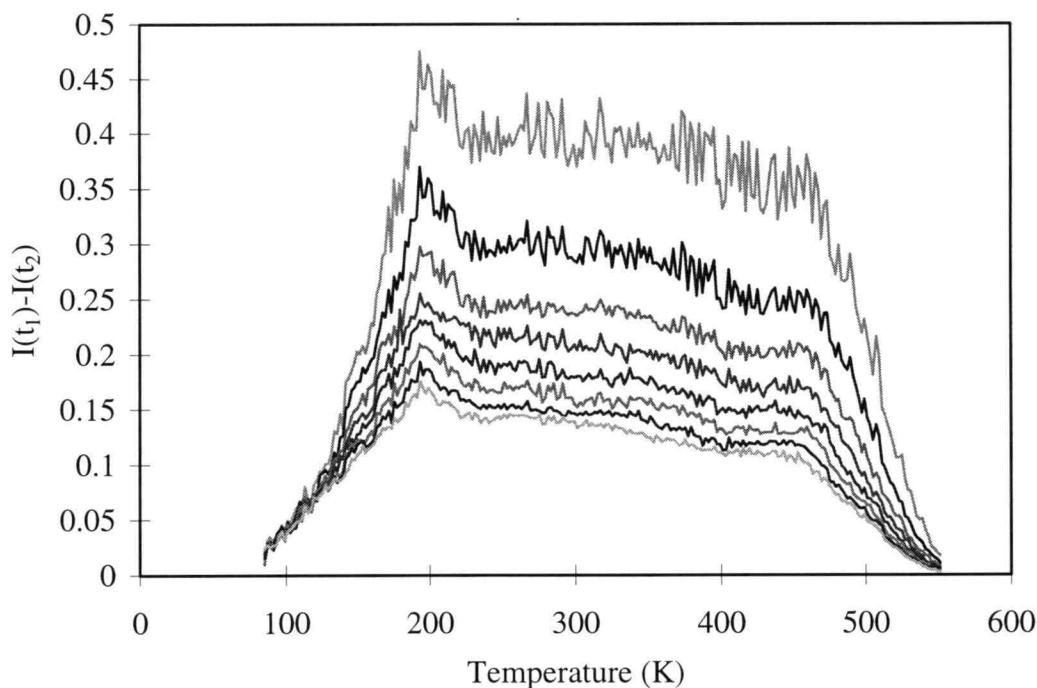


**Figure 5.10** Rate-window curves for an ALE SrS:Ce ACTFEL device. These curves were constructed using a constant  $t_1:t_2$  ratio of 1:10. The curves from top to bottom are for  $t_1:t_2$  times of 15:150, 20:200, 30:300, 40:400, 50:500, 60:600, 70:700, 80:800.

energies is most likely due to the large uncertainty in the experimental data that arises from the noisy signal. The Arrhenius analysis of peak B in Fig. 5.8 shows an activation energy of 2.04 eV and a capture cross-section of  $2.82 \times 10^{-4} \text{ cm}^2$ , as shown in Fig. 5.9(b). This is virtually identical to that found from TTL analysis.

The rate-window curves for the undoped sputtered SrS ACTFEL device which is doped with Ga are shown in Fig. 5.10. Note that the peak, which is readily visible in the TTL curves for this sample shown in Fig. 5.6, appears weakly as more of a shoulder than a peak in the rate-window curves. This peak is not resolvable using the rate-window method of data analysis. Reducing the amount of noise present in the rate-window curves would allow for a clear definition of the peak and thus an Arrhenius plot could be constructed. This clearly defines the need for better experimental methods, such as signal averaging, to reduce the amount of noise present in the data.

## 5.5 Summary

The traditional TTL experiment is successfully set up and conducted on an undoped sputtered SrS ACTFEL device which is doped with Ga and an ALE deposited SrS:Ce ACTFEL device. The TTL and DLTS analysis techniques has demonstrated that trap activation energies and capture cross-sections can be estimated using the luminescent decay curve. Both the TTL and the rate-window analysis must be proven by conducting careful, detailed studies of materials populated with well established defects. One or both of these methods may prove to be of importance in establishing the nature of traps in SrS ACTFEL devices processed in various manners.

The trap density in the phosphor can be estimated from the TTL peak intensity if it is assumed that the traps of interest are completely filled. Similarly the rate-window method can be used to estimate trap concentrations, assuming that the traps are completely filled. The filtered light source used in this study is not of sufficient intensity to completely fill the traps throughout the phosphor layer and thus the trap density cannot be estimated from these particular experiments. A higher intensity light source in future TTL or rate-window experiments will allow for accurate estimation of the observed trap density in the material. Once the experimental setup is operational, it is a simple task to take the data necessary to generate TTL and rate-window curves and the corresponding Arrhenius plots.

Future samples used in this work need to be specially constructed to eliminate any artificial responses that can be caused by unwanted dopants in the phosphor layer or by conducting the experiment through other deposited layers, such as the top insulator in a normal ACTFEL stack. This could be accomplished by depositing either SrS or SrS:Ce phosphor material directly onto quartz plates so that the experiment can be accomplished from the substrate side of the material, i.e. UV excitation pulses can be transmitted to the phosphor through the substrate without being absorbed in the substrate. The deposited material must be encapsulated due the reactivity of SrS based materials in normal atmosphere. If this is not feasible, then another scheme would be to deposit material in a manner that is typical of the process involved, then encapsulating the phosphor with a thin layer of a material that is transparent in the UV range.

Care must be taken when conducting the experiment at the temperature extremes minimize signal degradation. Perhaps the optimal solution to this problem is to place the PMT away from the quartz window of the environmental chamber in order to minimize PMT temperature variations.

## Chapter 6

# CONCLUSIONS AND RECOMMENDATIONS FOR FUTURE WORK

The principle contributions of this thesis are the electrical characterization of SrS:Ce ACTFEL devices grown by various methods, a successful demonstration of the traditional TTL experiment, and an extension of the DLTS rate-window concept to the analysis of luminescent decay curves. This chapter focuses on conclusions and recommendations for future work.

### 6.1 Conclusions

Comparison of the electrical characteristics of various SrS:Ce ACTFEL devices to an evaporated ZnS:Mn ACTFEL device through the use of C-V and Q-F<sub>p</sub> analysis, shows that the blue-green emitting SrS:Ce devices exhibit overshoot at turn-on, which is indicative of dynamic space-charge generation. In general, these devices exhibit no steady-state field and no field-clamping, which is also attributed to the generation of space-charge in the phosphor layer. Most of the devices observed indicate that a significant portion of carriers are generated from bulk states, as opposed to the evaporated ZnS:Mn ACTFEL device, in which a majority of the carriers are sourced from interface states. This is also consistent with generation of space charge by ionization of Ce in the phosphor layer. These same characteristics are observed for undoped SrS phosphors which indicate that dynamic space-charge generation is due in part to the ionization of native defects.

The transient thermoluminescent studies show that activation energies can be determined using phosphor thin-film material. A tentative identification of the activation energy of the Ce dopant is made using this method. Larger activation energies are also observed which may be related to native defects that give rise to the space-charge generation characteristics observed in undoped SrS ACTFEL devices.

## 6.2 Recommendations for Future Work

- (1) Electrical and brightness versus voltage (B-V) aging studies need to be performed for this class of material to provide more insight into the physics of the variously deposited SrS:Ce ACTFEL devices.
- (2) The temperature dependence of the electrical characteristics should be explored to determine if the mechanism responsible for space-charge generation is affected during electrical operation.
- (3) Maximum charge-maximum applied bias ( $Q_{\max}$ - $V_{\max}$ ) studies will give important information about basic device physics such as electron emission and capture processes and charge multiplication or impact ionization of impurities.
- (4) Space-charge generation increases the instantaneous power above that which would be measured for a similar device without space-charge generation. Power consumption studies are necessary to investigate these issues.
- (5) Explore the change in the observed space-charge characteristics with respect to variations in the applied frequency of the driving pulse. This will give insight into the time response of the mechanism responsible for space-charge generation. This data can be used to determine an optimal system frequency that minimizes power consumption.
- (6) Design samples that are better suited for the TTL and rate-window experiment. An example would be to deposit the phosphor onto bare quartz (i.e. a UV transparent material) and then cap with some suitable layer to prevent reaction of the SrS material with the atmosphere.
- (7) Refine the TTL experiment to control the temperature of the fixturing on the faceplate to prevent signal degradation from obscuring experimental results. This may also be accomplished by separating the PMT from the quartz window on the environmental chamber to provide for independent temperature control of the PMT and the quartz window of the environmental chamber.
- (8) Use signal averaging in the TTL experiment to provide cleaner data which will yield better resolution of peaks and shoulders in the TTL and rate-window

response curves. The determination of the intercept and thus the capture cross-section will be more reliable with cleaner data.

- (9) Use the TTL recommendations above to improve signal response to the point where luminescence from the material can be filtered with a monochromator to determine the spectral response that is associated with each peak and shoulder seen in the TTL or rate-window response curves.
- (10) A deeper investigation of TTL and/or the rate-window experiment to ensure that the techniques are reliable and accurate can be accomplished by performing the experiment using samples that have well established trapping states.

**BIBLIOGRAPHY**

- [1] W. A. Barrow, R. E. Coover, and C. N. King, "Strontium Sulphide: The Host for a new High Efficiency Thin Film EL Blue Phosphor," *Digest of the 1984 SID Int'l Display Symposium*, p.249, 1984.
- [2] S. P. Keller, J. E. Mapes, and G. Cheroff, "Studies on Some Infrared Stimulable Phosphors," *Phys. Rev.*, vol. 108, p. 663, 1957.
- [3] T. E. Peters and J. A. Baglio, "Luminescence and Structural Properties of Thiogallate Phosphor Ce and Eu - Activated Phosphors. Part I," *J. Elec. Soc.*, vol. 119, p. 230, 1970.
- [4] W. A. Barrow, R. E. Coover, E. Dickey, C. N. King, C. Laakso, S. S. Sun, R. T. Tuenge, R. Wentross, and J. Kane, "A New Class of Blue TFEL Phosphors with Applications to a VGA Full Color Display," *Digest of the 1993 SID Int'l Display Symposium*, p. 761, 1993.
- [5] L. V. Pham, "Electrical Characterization, Maximum Charge-Maximum Voltage ( $Q_{\max}$ - $V_{\max}$ ) Analysis, Aging and Temperature Studies of Thiogallate Thin-Film Electroluminescent Devices," MS Thesis, Oregon State University, 1995.
- [6] G. Destriau, "Recherches sur les Scintillations des Zinc aux Rayons," *J. de Chime Physique*, vol. 33, p. 587, 1936.
- [7] M. J. Russ and D. I. Kennedy, "The Effects of Double Insulating Layers on the Electroluminescence of Evaporated ZnS:Mn Films," *J. Electrochem. Soc.*, vol. 114, p. 1066, 1967.
- [8] T. Inoguchi, M. Takeda, Y. Kakihora, and M. Yoshida, "Stable High Luminance Thin-Film Electroluminescent Panels," *Digest of the 1974 SID Int'l Display Symposium*, p. 86, 1974.
- [9] S. Freed, "Electronic Transition Between an Inner Shell and the Virtual Outer Shells of the Ions of the Rare Earths in Crystals," *Phys. Rev.*, vol. 38, p. 2122, 1931.

- [10] S. P. Keller, "Fluorescence Spectra, Term Assignments, and Crystal Field Splittings of Rare Earth Activated Phosphors," *J. Chem. Phys.*, vol. 29, p. 180, 1958.
- [11] A. A. Douglas, J. F. Wager, D. C. Morton, J. B. Koh, and C. P. Hough, "Evidence for space charge in atomic layer epitaxy ZnS:Mn alternating-current thin-film electroluminescent devices," *J. Appl. Phys.*, vol. 73, p. 296-299, 1993.
- [12] A. Abu-Dayah, J. F. Wager, and S Kobayashi, "Electrical Characterization of Atomic Layer Epitaxy ZnS:Mn Alternating-Current Thin-Film Electroluminescent Devices Subject to Various Waveforms," *J. Appl. Phys.*, vol. 74, p. 5575-5581, 1993.
- [13] A. A. Douglas, "Alternating-Current Thin-Film Electroluminescent Device Physics and Modeling," MS Thesis, Oregon State University, 1993.
- [14] S. Wolf and R. N. Tauber, *Silicon Processing for the VLSI Era Vol. 1*, Lattice Press, California, 1986.
- [15] R. Glang, "Vacuum Evaporation," in L. Maissel and R. Glang, Eds., *Handbook of Thin Film Technology*, McGraw-Hill, New York, Ch. 1, p. 1-130, 1970.
- [16] C. H. L. Goodman and M. V. Pessa, "Atomic Layer Epitaxy," *J. Appl. Phys.*, vol. 60, p. , 1986.
- [17] S. H. Sohn and Y Hamakawa, "A Model for Emission from ZnS:Ce<sup>3+</sup> and SrS:Ce<sup>3+</sup> Thin-Film Electroluminescent Devices," *Jpn. J. Appl. Phys.*, vol. 31, p. 3901, 1992.
- [18] S. Tanaka, "Thin-Film Electroluminescent Devices Using CaS and SrS" *J. Cryst. Growth*, vol. 101, p. 958, 1990.
- [19] R. Crandall and M. Ling, "Evidence for Recombination-Controlled Electroluminescence in Alkaline-Earth Sulfides," *J Appl. Phys.*, vol. 62, p. 3074, 1987.
- [20] K. Ohmi, K. Ishitani, Y. Kashio, S. Tanaka, and H. Kobayashi, "Characterization of Electrical Properties of SrS:Ce," *presented at the First Int'l.*

*Conf. on the Sci. and Tech. of Display Phosphors*, San Diego, CA, Nov. 14-16, 1995.

- [21] B. Huttli, U. Troppenz, K. O. Velthaus, C. R. Ronda, and R. H. Mauch, "Luminescence Properties of SrS:Ce<sup>3+</sup>," *J. Appl. Phys.*, vol. 78, p. 7282, 1995.
- [22] Y. A. Ono, M. Fuyama, K. Onisawa, and K. Tamura, "White-light Emitting Thin Film Electroluminescent Devices with Stacked SrS:Ce/CaS:Eu Active Layers," *J. Appl. Phys.*, vol. 66, p. 5564, 1989.
- [23] K. Ohmi, S. Inoue, S. Tanaka, and H. Kobayashi, "Relaxation of Phosphor Field in SrS:Ce Thin Film Electroluminescent Devices," *Appl. Phys. Lett.*, vol. 64, p.3464, 1994.
- [24] K. Ohmi, K. Fujimoto, S. Tanaka, and H. Kobayashi, "Improvement of Crystallographic and Electroluminescent (EL) Characteristics of SrS:Ce Thin Film EL Devices by Post-Deposition Annealing in Ar-S Atmosphere," *J. Appl. Phys.*, vol. 78, p. 428, 1995.
- [25] R. Helbing and R. S. Feigelson, "Growth of SrS Single Crystals by Physical Vapor Transport," *J. Cryst. Growth*, vol. 137, p. 150, 1994.
- [26] R. H. Mauch, K. O. Velthaus, G. Bilger, and H. W. Schock, "High Efficiency SrS,SrSe:CeCl<sub>3</sub> Based Thin Film Electroluminescent Devices," *J. Cryst. Growth*, vol.117, p. 964, 1992.
- [27] K. Onisawa, T. Yoshimi, K. Nakamura, T. Kobayashi, S. Sato, and S. Miura, "" *Jpn. J. Appl. Phys.*, vol. 28, p. 1378, 1989.
- [28] M. Takeda, Y. Kanatani, H. Kishishita, T. Inoguchi, and K. Okano, *Digest of the 1980 SID Int'l Display Symposium*, p. 66, 1980.
- [29] D. H. Smith, "Modeling a.c. Thin-Film Electroluminescent Devices," *J Lum.*, vol. 23, p. 209, 1981.
- [30] J. D. Davidson, J. F. Wager, I. Khormaei, C. N. King, R. Williams, "Electrical Characterization and modeling of Alternating-Current Thin-Film

- Electroluminescent Devices," *IEEE Trans. on Elect. Dev.*, vol. 39, no. 5, p. 1122, 1992.
- [31] J. D. Davidson, "Capacitance-Voltage Analysis, SPICE Modeling, and Aging Studies of AC Thin-Film Electroluminescent Devices," MS Thesis, Oregon State University, 1991.
- [32] P. D. Keir, "Modeling Phosphor Space Charge in Alternating-Current Thin-Film Electroluminescent Devices," MS Thesis, Oregon State University, 1995.
- [33] R. C. McArthur, J. D. Davidson, J. F. Wager, I. Khormaei, C. N. King, "Capacitance-Voltage characteristics of Alternating-Current Thin Film Electroluminescent Devices," *Appl. Phys. Lett.*, vol. 56, p. 1889, 1990.
- [34] J. F. Wager, A. A. Douglas, and D. C. Morton, "Electrical Characterization and Modeling of ACTFEL Devices," *Electroluminescence, Edited by V. P. Singh and J. C. McClure*, Cinco Puento Press, El Paso, p. 92, 1992.
- [35] A. Abu-Dayah, J. F. Wager, and S Kobayashi, "Internal Charge-Phosphor Field Characteristics of Alternating-Current TFEL Devices," *Appl. Phys. Lett.*, vol. 62, p. 744, 1993.
- [36] C. B. Sawyer and C. H. Tower, "Rochelle Salt as a Dielectric," *Phys. Rev.*, vol. 35, p. 269, 1930.
- [37] E. Bringuier and A. Geoffrey, *Appl. Phys. Lett.*, vol. 60, p. 1256, 1992.
- [38] A. A. Douglas and J. F. Wager, "ACTFEL Device Response to Systematically Varied Pulse Waveforms," *Electroluminescence, Edited by V. P. Singh and J. C. McClure*, Cinco Puento Press, El Paso, p. 387, 1992.
- [39] R. S. Crandall, "Mechanism of Electroluminescence in Alkaline-Earth Sulfides," *Appl. Phys. Lett.*, vol. 50, p. 551, 1987.
- [40] K. Ohmi, K. Ishitani, S. Tanaka, and H. Kobayashi, "Role of Space Charge in SrS:Ce Thin-Film Electroluminescent Devices Studied by the Photoirradiation Effect," *Appl. Phys. Lett.*, vol. 67, p. 944, 1995.

- [41] S. Tanaka, H. Yoshiyama, K. Nakamura, S. Wada, H. Morita, H. Kobayashi, "Photo-Induced Transferred charge in Rare-Earth-Doped Alkaline-Earth Sulfide Electroluminescent Thin Films," *Jpn. J. Appl. Phys.*, vol. 30, p. L1021, 1991.
- [42] R. Thuemler, P. D. Keir, and J. F. Wager, "Phosphor Field Dependence in ALE SrS:Ce ACTFEL Devices", *SID Digest 1995*, p. 473 , 1995.
- [43] E. Nakazawa, "A New Method for the Characterization of Traps in Luminescent Materials," *Jpn. J. Appl. Phys.*, vol. 23, p. L755, 1984.
- [44] J. Rennie, E. Nakazawa, and T. Koda, "Trapping States in CaS and SrS Single Crystals, Films, and Powders as Revealed Using the Technique of Transient Thermoluminescence," *Jpn. J. Appl. Phys.*, vol. 29, p. 509, 1990.
- [45] W. Hoogenstraaten, *Phillips Res. Rept.*, vol. 13, p. 515, 1958.
- [46] P. Kivits and H. J. L. Hagebeuk, *J. Lum.*, vol. 15, p. 1, 1977.
- [47] J. F. Wager, "Electrical Characterization of Deep Levels in Semiconductors," *Unpublished seminar notes*.
- [48] J. F. Wager, "Static Space Charge," *Unpublished notes*, November 24, 1995.
- [49] D. V. Lang, "Deep-Level Transient Spectroscopy: A New Method to Characterize Traps in Semiconductors," *J. Appl. Phys.*, vol. 45, p. 3023, 1974.
- [50] A. Hasegawa and A. Yanase, *J. Phys. C*, vol. 13, p. 1995, 1980.